


RESEARCH ARTICLE OPEN ACCESS

Automated MRI Segmentation of Brainstem Nuclei Critical to Consciousness

Mark D. Olchanyi^{1,2,3}  | Jean Augustinack⁴ | Robin L. Haynes⁵ | Laura D. Lewis^{3,4,6} | Nicholas Cicero^{3,7} | Jian Li^{2,4} | Christophe Destrieux^{8,9} | Rebecca D. Folkerth¹⁰ | Hannah C. Kinney⁵ | Bruce Fischl¹⁴ | Emery N. Brown^{1,3} | Juan Eugenio Iglesias^{4,11,12} | Brian L. Edlow^{2,4}

¹Neuroscience Statistics Research Laboratory, Massachusetts Institute of Technology, Cambridge, Massachusetts, USA | ²Center for Neurotechnology and Neurorecovery, Department of Neurology, Massachusetts General Hospital, Boston, Massachusetts, USA | ³Institute for Medical Engineering and Sciences, Massachusetts Institute of Technology, Cambridge, Massachusetts, USA | ⁴Athinoula A. Martinos Center for Biomedical Imaging, Department of Radiology, Massachusetts General Hospital, Charlestown, Massachusetts, USA | ⁵Department of Pathology, Boston Children's Hospital, Boston, Massachusetts, USA | ⁶Department of Electrical Engineering and Computer Science, Massachusetts Institute of Technology, Cambridge, Massachusetts, USA | ⁷Graduate Program for Neuroscience, Boston University, Boston, Massachusetts, USA | ⁸UMR 1253, iBrain, Université de Tours, Tours, France | ⁹CHRU de Tours, 2 Boulevard Tonnellé, Tours, France | ¹⁰Brain Injury Research Center, Icahn School of Medicine at Mount Sinai, New York, New York, USA | ¹¹Centre for Medical Image Computing, University College London, London, UK | ¹²Computer Science and Artificial Intelligence Laboratory, Massachusetts Institute of Technology, Cambridge, Massachusetts, USA

Correspondence: Brian L. Edlow (bedlow@mgh.harvard.edu)

Received: 4 October 2024 | **Revised:** 3 September 2025 | **Accepted:** 8 September 2025

Funding: This work was supported by NIH Director's Office (DP2 HD101400), NIH National Institute of Neurological Disorders and Stroke (R01NS128961, R21NS109627, RF1NS115268, U01NS086625, U01NS132181, U01NS137484, U24NS135561, U54NS115322), NIH National Institute of Mental Health (RF1MH123195), NIH National Institute of Biomedical Imaging and Bioengineering (T32EB001680), US Department of Defense (W81XWH2210999), NIH National Institute on Aging (R01AG070988, U19AG024904), Alzheimer's Research UK Interdisciplinary Grant (ARUK-IRG2019A-003), European Research Council Starting Grant (677697), Rappaport Foundation, MIT-Takeda Fellowship, James S. McDonnell Foundation, MIT/MGH Brain Arousal State Control Innovation Center (BASCIC) Project, and the Chen Institute MGH Research Scholar Award.

Keywords: arousal | atlas | brainstem | consciousness | ex vivo MRI | histology | segmentation

ABSTRACT

Although substantial progress has been made in mapping the connectivity of cortical networks responsible for conscious awareness, neuroimaging analysis of subcortical networks that modulate arousal (i.e., wakefulness) has been limited by a lack of robust segmentation procedures for ascending arousal network (AAN) nuclei in the brainstem. Automated segmentation of brainstem AAN nuclei is an essential step toward elucidating the physiology of human consciousness and the pathophysiology of disorders of consciousness. We created a probabilistic atlas of 10 AAN nuclei built on diffusion MRI scans of 5 ex vivo human brain specimens imaged at 750 μm isotropic resolution. The neuroanatomic boundaries of AAN nuclei were manually annotated with reference to 200 μm 7 Tesla MRI scans in all five specimens and nucleus-specific immunostains in two of the scanned specimens. We then developed a Bayesian segmentation algorithm that utilizes the probabilistic atlas as a generative model and automatically identifies AAN nuclei in a resolution- and contrast-adaptive manner. The segmentation method displayed high accuracy when applied to in vivo T1 MRI scans of healthy individuals and patients with traumatic brain injury, as well as high test-retest reliability across T1 and T2 MRI contrasts. Finally, we show through classification and correlation assessments that the algorithm can detect volumetric changes and differences in magnetic susceptibility within AAN nuclei in patients with Alzheimer's disease and traumatic coma, respectively. We release the probabilistic atlas and Bayesian segmentation tool to advance the study of human consciousness and its disorders.

The last two authors are co-senior authors.

This is an open access article under the terms of the [Creative Commons Attribution-NonCommercial-NoDerivs](https://creativecommons.org/licenses/by-nc-nd/4.0/) License, which permits use and distribution in any medium, provided the original work is properly cited, the use is non-commercial and no modifications or adaptations are made.

© 2025 The Author(s). *Human Brain Mapping* published by Wiley Periodicals LLC.

1 | Introduction

Over the past two decades, connectivity studies of cortical networks have begun to reveal the structural and functional correlates of human cognition (Buckner and DiNicola 2019; Glasser et al. 2016; Yeo et al. 2011). Observations about the spatial and temporal dynamics of cortical network connectivity (Fox et al. 2005; Horn et al. 2014; Sporns et al. 2005) have yielded insights into the neuroanatomic basis of language, memory, attention, emotion, and conscious awareness (Cole et al. 2014; Demertzi et al. 2019; Glasser et al. 2016; Medaglia et al. 2015). In parallel, network-based models of neuropsychiatric diseases have emerged, based on the observation that spatially disparate lesions can cause cognitive deficits and behavioral dysfunction by disrupting a shared network architecture (Bodien et al. 2017; Boes et al. 2015; Fischer et al. 2016; Snider, Hsu, et al. 2020).

Yet as cortical connectivity mapping has accelerated, progress in mapping the subcortical networks that modulate arousal (i.e., wakefulness) has lagged behind. Few studies have attempted to map the complex connectivity of brainstem networks (Beissner et al. 2014; Bianciardi et al. 2016; Edlow et al. 2012, 2016, 2024; Hansen et al. 2024; Li et al. 2021; Sclocco et al. 2018). As a result, fundamental questions about the pathogenesis of a broad range of disorders of arousal, including coma (Edlow et al. 2021), sudden infant death syndrome (Kinney and Haynes 2019), and post-COVID-19 fatigue (Huang et al. 2021) remain unanswered. This gap in knowledge is partly attributable to the lack of robust and automated methods for segmenting the brainstem regions that comprise the ascending arousal network (AAN).

The brainstem AAN is made up of at least 10 neurotransmitter-specific regions (nuclei) that modulate arousal and ultimately consciousness (Edlow et al. 2012; Parvizi 2001; Valenza et al. 2019). These regions, which our proposed algorithm segments, are the (predominantly) serotonergic dorsal raphe (DR) and median raphe (MnR), the noradrenergic locus coeruleus (LC), the cholinergic laterodorsal tegmental nucleus (LDTg) and pedunculotegmental nucleus (PTg), the glutamatergic parabrachial complex (PBC), pontis oralis (PnO) and midbrain reticular formation (mRt), the dopaminergic ventral tegmental area (VTA), and the multi-neurotransmitter periaqueductal gray (PAG). We henceforth refer to these 10 regions as AAN nuclei. Beyond arousal, these AAN nuclei are also central to many vital functions of the brainstem, including respiration (Chamberlin and Saper 1994), sleep/circadian rhythm generation (Saper et al. 2005) and pain modulation (Mayer et al. 1971; Reynolds 1969).

To date, brainstem segmentation methods have mainly focused on the brainstem as a whole. The brainstem is extracted by segmentation modules of most neuroimaging packages, such as “aseg” (Fischl et al. 2002) in FreeSurfer (Fischl 2012) or FIRST (Patenaude et al. 2011) in FSL (Smith et al. 2004). The whole brainstem has also been targeted in multi-atlas segmentation methods (Heckemann et al. 2006), as well as specifically designed methods, such as (Bondiaou et al. 2005) based on a single labeled template, or (Lee et al. 2005, 2007) based on active contours.

Beyond whole-brainstem segmentation, several methods have segmented the brainstem into its three main neuroanatomic components—the medulla, pons, and midbrain—based on manual procedures (Lechanoine et al. 2021), geometric rules (Nigro et al. 2014) or Bayesian methods (Ashburner and Friston 2005; Iglesias, Van Leemput, et al. 2015; Lambert et al. 2013). However, automated segmentation techniques for individual brainstem nuclei beyond simple registration to a single labeled template (e.g., the Harvard AAN Atlas) (Edlow et al. 2012, 2024) have not yet been developed. Recently, several teams of investigators leveraged ultra-high resolution imaging datasets to provide anatomic atlases of brainstem nuclei (Adil et al. 2021; Bianciardi 2021; Lechanoine et al. 2021), but these atlases do not segment all of the miniscule brainstem nuclei in the pontine and midbrain tegmentum that are critical to arousal and homeostasis.

Here, we develop a probabilistic brainstem AAN atlas from manual tracings made on ex vivo MRI data acquired in five human brain specimens at 750 μ m resolution, guided by 200 μ m 7Tesla (7 T) MRI scans in all five specimens and nucleus-specific immunostains in two of the scanned specimens. Ex vivo MRI provides substantial improvements in signal-to-noise ratio and spatial resolution over in vivo MRI by reducing motion and enabling long scanning times (Edlow et al. 2019; McNab et al. 2009; Yendiki et al. 2022). These high-resolution ex vivo images facilitate precise manual delineation of AAN structures, which in turn enable building an atlas with a superior level of detail.

We then used the new probabilistic version of the Harvard AAN Atlas as the basis for the creation of a companion automated algorithm that segments AAN brainstem arousal nuclei with in vivo MRI. The segmentation algorithm is based on Bayesian inference using generative models of brain MRI data (Ashburner and Friston 2005; Van Leemput et al. 1999; Pohl et al. 2006; Wells et al. 1996). Because the modeling of intensities is unsupervised, this approach allows investigators to apply atlases built in ex vivo brain specimens to the segmentation of in vivo MRI scans (Iglesias, Augustinack, et al. 2015; Iglesias et al. 2018; Saygin et al. 2017).

To demonstrate the translational potential of this automated segmentation tool, we apply it to a volumetric analysis of AAN brainstem nuclei in patients with Alzheimer’s disease (AD) and hemorrhagic lesion intensity analysis acute traumatic disorders of consciousness (DoC), as compared to healthy human subjects. We release the AAN automated segmentation tool, which we term **AANSegment**, as part of the FreeSurfer neuroimaging package to facilitate a broad range of potential applications in the study of human consciousness and its disorders.

2 | Methods

2.1 | Ex Vivo Brain Specimen Overview

We analyzed five human brain specimens: two using histological sectioning (S1, S2) and all using ex vivo MRI (S1, S2, S3, S4, S5). All brains were donated by individuals with no history

TABLE 1 | Demographics and details on postmortem fixation for all ex vivo brain specimens.

Specimen number	Age	Sex	Medical history	Cause of death	Postmortem fixation interval (h)	Fixative	Fixation-to-imaging duration (M)	Histology included
1	60	F	Cecal adenocarcinoma (metastatic), DVT, depression	Septic shock	< 24	10% formalin	24	Yes
2	61	F	HTN, ovarian cancer (metastatic)	Septic shock	72	10% formalin	20	Yes
3	50	M	Depression, leukemia, Raynaud's phenomena, thromboembolism	DIC due to hemophagocytic lymphohistiocytosis	< 24	10% formalin	93	No
4	58	F	Breast cancer, ulcerative colitis	PE and/or DAD in the setting of widely metastatic breast cancer	< 24	10% formalin	92	No
5	83	M	Hyperlipidemia, chronic respiratory deficiency	Acute respiratory failure	23	5% formalin	50	No

Abbreviations: DAD, diffuse alveolar damage; DIC, disseminated intravascular coagulation; DVT, deep vein thrombosis; HTN, hypertension; PE, pulmonary embolism.

of neurological disease and who died of non-neurological causes. Consent for brain donation and research was provided by surrogate decision-makers as part of protocols approved by the Institutional Review Boards at Mass General Brigham (S1–S3) or at the Université de Tours (S4, S5). Postmortem examination of each brain specimen by a neuropathologist was grossly normal.

Brain specimens were extracted from the cranium and fixed in 10% formalin (S1–S4) or 5% formalin (S5) for at least 20 months prior to ex vivo MRI. Immediately prior to scanning, all specimens were transferred to a fomblin solution (Solvay Specialty Polymers, Bollate, Italy) to reduce artifacts related to magnetic susceptibility, as previously described (Edlow et al. 2019). Specimen demographics, causes of death, and fixation parameters are summarized in Table 1.

2.2 | Data Acquisition

2.2.1 | Ex Vivo MRI







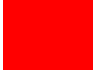



Each ex vivo brain specimen (S1–S5) was scanned on a 7 Tesla (7T) Siemens Magnetom scanner and a 3T Siemens Tim Trio scanner (Siemens Healthineers, Erlangen, Germany). The 7T Fast Low-Angle SHot (FLASH) sequence (Augustinack et al. 2005; Fischl et al. 2004) utilized the following parameters: TR = 40 ms, TE = 14.2 ms, flip angle = 20°, acquired at 200 μ m isotropic spatial resolution. The 3T diffusion-weighted steady-state free precession (DWSSFP) sequence (McNab et al. 2009) utilized the following parameters: TR = 38 ms, TE = 23 ms, flip

angle = 60°, with 90 diffusion-encoding directions at an effective gradient strength of $b = 3773 \text{ s/mm}^2$ and 12 low- b images (where $b = 0 \text{ s/mm}^2$) acquired at 750 μ m isotropic spatial resolution.

2.2.2 | Histology and Immunostaining

The two specimens that underwent histological analysis (S1, S2) were sectioned and stained in the axial (i.e., transverse) plane using a standardized protocol, as previously described (Edlow et al. 2024). Briefly, the brainstem was dissected from the brain specimen via a transverse cut at the mesencephalic-diencephalic junction. Each brainstem was then separated into four blocks (medulla, caudal pons, rostral pons, and midbrain), which were embedded in paraffin. Serial sections were cut at 10 μ m thickness from the paraffin-embedded blocks using a microtome (LEICA RM2255 microtome, Leica Microsystems, Buffalo Grove, IL, USA). Every 250 μ m, a section was stained with hematoxylin and eosin and counterstained with Luxol fast blue (H&E/LFB) for identification of cell bodies and myelin. Sections were then selected based on anatomic landmarks to identify brainstem arousal nuclei at the level of the rostral pons (PnO, MnR, LC, PBC, LDTg), caudal midbrain (mRt, VTA, PTg, DR, PAG) and rostral midbrain (mRt, VTA, and PAG). Tyrosine hydroxylase immunostaining was used to identify the VTA and LC, tryptophan hydroxylase staining to identify the MnR and DR, and H&E/LFB to identify the PnO, LC, PBC, LDTg, PTg, and PAG. A summary of the brainstem arousal nuclei that were assessed, along with their immunostaining and histological characteristics, is provided in Table 2. All histological sections were digitized with the NanoZoomer S60 Digital Slide Scanner

TABLE 2 | Description of AAN nuclei, including their primary neurotransmitter-specific cell bodies, histological staining, and corresponding locations for manual annotation.

Brainstem arousal nucleus	Abbreviation	ROI color	Primary neurotransmitter	Histology and immunohistochemistry	Volume of nucleus (voxels)	Volume of nucleus (mm ³)
Dorsal raphe	DR		Serotonin	Positive staining for tryptophan hydroxylase	429	181.2
Median raphe	MnR		Serotonin	Positive staining for tryptophan hydroxylase	191	8.6
Locus coeruleus	LC		Norepinephrine	Positive staining for tyrosine hydroxylase and visible on H&E-LFB	101	42.7
Laterodorsal tegmental nucleus	LDTg		Acetylcholine	Annotated with H&E-LFB	37	15.7
Parabrachial complex	PBC		Glutamate	Annotated with H&E-LFB	170	71.6
Pontis oralis	PnO		Glutamate	Annotated with H&E-LFB	372	156.9
Midbrain reticular formation	mRt		Glutamate	Annotated with H&E-LFB	1079	455.1
Pedunculotegmental nucleus	PTg		Acetylcholine	Annotated with H&E-LFB	298	125.6
Periaqueductal gray	PAG		Multiple	Annotated with H&E-LFB	850	358.4
Ventral tegmental area	VTA		Dopamine	Positive staining for tyrosine hydroxylase	680	287.0

Note: Nucleus volumes and voxel counts (in terms of native 0.7 mm isotropic voxels in low-*b* space) were derived from averaging over manual annotations from each ex vivo brain specimen used for atlas construction. ROI colors are consistent with the colors used in the Harvard Ascending Arousal Network template (Edlow et al. 2012, 2024).

(Hamamatsu Photonics). Digitized slides underwent a custom whole-slide image processing pipeline for white balance correction and contrast enhancement. We converted all histological slides to JPEG2000 format and previously released them through the Biolucida platform (MBF Bioscience) for visualization.

2.2.3 | In Vivo MRI of Traumatic Brain Injury Patients

We utilized in vivo MRI data from 10 healthy control subjects and 18 patients with severe traumatic brain injury (TBI). The patients with severe TBI were scanned during the acute phase of injury in the intensive care unit as part of a previously published observational study at Massachusetts General Hospital (Edlow et al. 2017). Informed consent was obtained from the healthy control subjects and from surrogate decision-makers for the patients with severe TBI, in accordance with a protocol approved by the Mass General Brigham Institutional Review Board. Healthy controls had no history of neurological, psychiatric, or medical diseases. Pertinent inclusion criteria for patients with acute severe TBI were: a Glasgow Coma Scale (GCS) (Teasdale and Jennett 1974) score of less than or equal to 8 without eye opening for at least 24 h post-injury and age 18–65 years. Individual subject information for the control and TBI cohorts can be found in Tables S1 and S2.

MRI data for all healthy subjects and patients with TBI were acquired on a 3T Siemens Skyra scanner (Siemens Medical

Solutions, Erlangen, Germany) using a 32-channel head coil. T1-weighted data were acquired using a MultiEcho Magnetization-Prepared Rapid Gradient Echo (MEMPRAGE) sequence (TR = 2530 ms, TE = 1.69/3.55/5.41/7.27 ms, flip angle: 7°) at 1 mm isotropic spatial resolution. A 3D susceptibility-weighted imaging (SWI) sequence (TR = 30 ms, TE = 20 ms, flip angle = 15°) was acquired for each subject at 0.86 × 0.86 × 1.8 mm spatial resolution.

2.2.4 | Alzheimer's Disease Data

All T1 MRI data used for AD analysis was obtained from the Alzheimer's Disease Neuroimaging Initiative (ADNI) database (adni.loni.usc.edu). The ADNI was launched in 2003 as a public-private partnership, led by Principal Investigator Michael W. Weiner, MD. The original goal of ADNI was to test whether serial magnetic resonance imaging, positron emission tomography, other biological markers, and clinical and neuropsychological assessment can be combined to measure the progression of mild cognitive impairment and early AD. Specifically, we used T1 MRI images (scanned at approximately 1 mm isotropic resolution) from 168 randomly-chosen subjects with AD (mean age: 75.53 ± 7.38, 80 females) and 215 age-matched control subjects (mean age: 76.09 ± 5.43, 96 females). AD subjects in this study were defined by ADNI as having (1) subjective memory complaints, (2) a score of 20–26 on the Mini Mental State Examination, (3) a Clinical Dementia Rating score of 0.5

or 1 with a memory box score of 0.5 or greater, (4) delayed recall of one paragraph from the Wechsler Memory-Scale Revised Logical Memory 2 subscale dependent on education level, and (5) met the National Institute of Neurological Disorders and Stroke–Alzheimer's Disease and Related Disorders Association probable AD criteria (Petersen et al. 2010). Further clinical and imaging acquisition information for each subject can be found at adni.loni.usc.edu. All aforementioned ADNI subjects were used in previous classification analyses (Iglesias, Augustinack, et al. 2015; Saygin et al. 2017).

2.2.5 | Human Connectome Project Data

We used 45 subjects from the Human Connectome Project (HCP) WU-Minn 1200 subject release dataset (Van Essen et al. 2013) who underwent two separate scanning sessions (included as part of the “Retest Data” cohort) with the same scanning protocols to assess test–retest reliability. Specifically, we analyzed unprocessed T1-weighted (TR = 2400 ms, TE = 2.14 ms, flip angle = 8°) and T2-weighted (TR = 3200 ms, TE = 565 ms, flip angle = 120°) MRI scans at 0.7 mm isotropic resolution. Further information can be found at db.humanconnectome.org.

2.3 | Ex Vivo Manual Annotation of Brainstem Arousal Nuclei

For ex vivo brain specimens with corresponding histological sections (S1, S2), AAN nuclei were traced on the DWSSFP 750 μ m average low-*b* image, which was directly used for probabilistic atlas construction, as described in Section 2.5.2. AAN nuclei in two specimens (S1, S2) were manually annotated in diffusion space for a prior study (Edlow et al. 2024); hence we performed manual annotations on diffusion low-*b* images for all specimens to maintain consistency. Tracing on the low-*b* image was performed with guidance from the 7T 200 μ m FLASH images, which provided contrast for the boundaries of smaller AAN nuclei. Although larger AAN nuclei such as the PAG, mRt, DR, and MnR possess sufficient contrast to annotate directly in the low-*b* images, the location and morphology of smaller neighboring AAN nuclei are inferred in low-*b* space directly from FLASH space.

AAN nuclei labels were further refined in two of the ex vivo brain specimens (S1, S2) with tyrosine hydroxylase (for VTA and LC staining), tryptophan hydroxylase (for DR and MnR staining), and H&E/LFB (for all other AAN nuclei) to aid in translating the location and morphology of the nuclei from (ground-truth) histological to low-*b* space. Representative annotations of AAN nuclei for an ex vivo brain specimen in histological, FLASH and low-*b* space, as well as for an in vivo T1 scan, are illustrated in Figure 1. Manual tracing of AAN nuclei in ex vivo brain specimens without histological sections (S3–S5) was performed with guidance from the 7T 200 μ m FLASH images, for which correlations between histological and MR contrast boundaries were extrapolated from S1 and S2. Specifically, for each specimen we observed that in the midbrain, the PAG, mRt, PTg and VTA all possess

hyperintense FLASH contrast with respect to the hypointense contrast of the red nuclei, cerebral peduncles and tegmental white matter. In the pons, the LC is a distinct region with hypointense FLASH contrast, the MnR is a hyperintense region along the tegmental midline, and the PBC is observed as a pair of hyperintense bands medial and lateral to the superior cerebellar peduncles. We have found that the neuroanatomic boundaries for the remaining AAN nuclei (PnO, LDTg, and DR) can be directly inferred based on the location of adjacent nuclei with observable FLASH contrast. Specifically, the location of the PnO can be inferred from the lateral borders of the MnR; the location of the LDTg from the ventro-medial borders of the LC; and the location of the DR from the dorsal border of the MnR and the dorsal/caudal border of the PAG. Representative contrast boundaries between histological space and FLASH space are illustrated in Figure S1. For all annotations, we also cross-referenced the neuroanatomic boundaries of each AAN nucleus with the Harvard Disorders of Consciousness Histopathology Collection (<http://histopath.nmr.mgh.harvard.edu>) and the Paxinos human brainstem atlas (Paxinos et al. 2012). Details regarding the annotation protocol and anatomic locations of AAN nuclei have been previously described (Edlow et al. 2024).

2.4 | In Vivo Manual Annotation of Brainstem Arousal Nuclei for Accuracy Assessment

To assess the accuracy of Bayesian segmentations on in vivo structural MRI scans in healthy brainstems and in the setting of structural brainstem injury, a neuroanatomy expert (M.D.O.) manually annotated all AAN nuclei from in vivo T1-weighted MRI scans in the 10 healthy control subjects and 10 patients from the TBI dataset. For the latter scans, we randomly chose a subset of 10 TBI patients who had either significant deformation of the brainstem due to increased intraventricular pressure and/or herniation, or hemorrhagic lesions in the brainstem on the T1-weighted image and corresponding SWI. The sensitivity of SWI to hemorrhagic lesions is illustrated in Figure S2.

Manual annotation was performed directly on the T1 images at 1 mm isotropic resolution. Similar to ex vivo specimens without corresponding histology, in vivo annotations first relied on direct localization of nuclei with observed T1 contrast, such as the PAG, mRt, VTA, DR, and MnR. Annotation of smaller, neighboring AAN nuclei with no reliable T1 contrast was performed with guidance from the Harvard AAN atlas, a previously published AAN delineation protocol (Edlow et al. 2012, 2024), and neuroanatomic boundaries from adjacent, more easily discernable AAN nuclei and brainstem structures from the Paxinos brainstem atlas (Paxinos et al. 2012). A representative T1 scan with illustrated steps of the in vivo manual annotation procedure is shown in Figure S3. A neuropathologist (H.C.K.) and neurologist (B.L.E.) with expertise in brainstem anatomy confirmed the neuroanatomic location of each annotation. We upsampled the manual AAN nuclei labels to the resolution of the automated segmentation generated by the Bayesian algorithm (0.4 mm) to compare manual annotations to automated segmentations in the same imaging space.

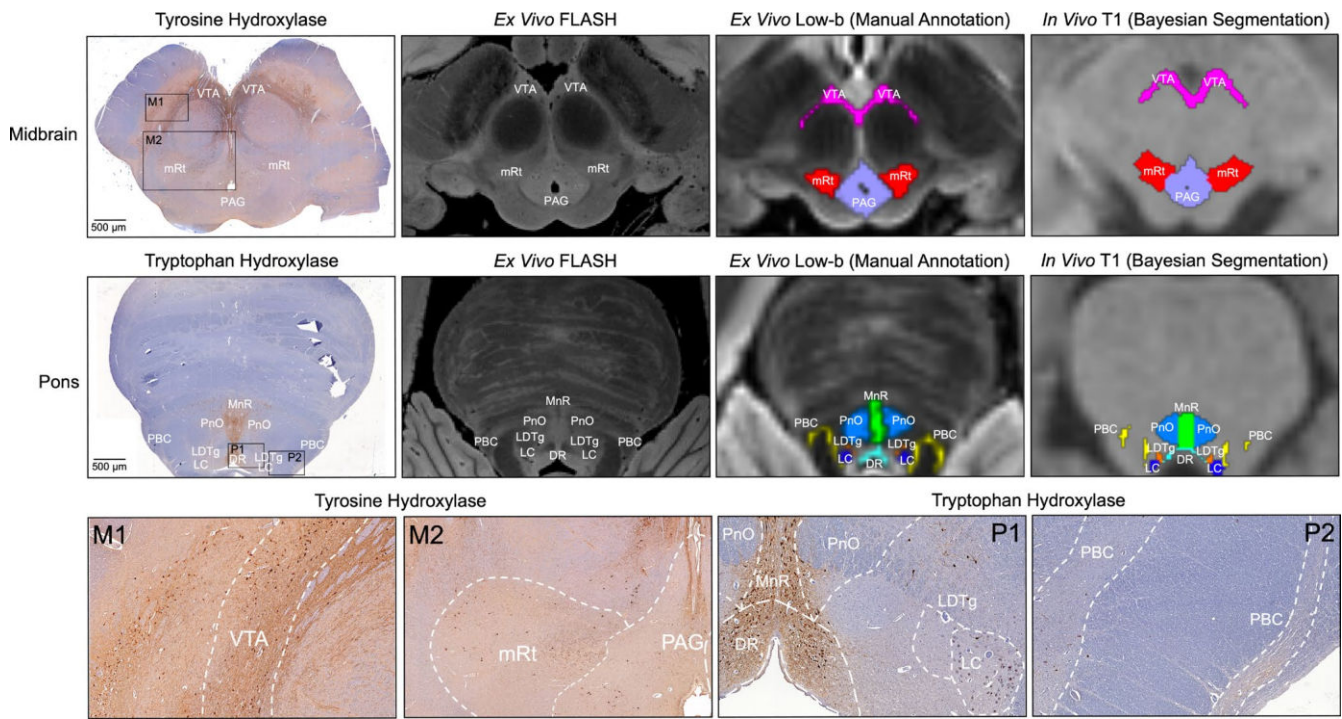


FIGURE 1 | Histology-imaging correlations of AAN nuclei. Corresponding histological sections (first column) and/or 200µm FLASH images (second column) were used for manually annotating AAN nuclei in 750µm low-*b* diffusion MRI images from ex vivo brain specimens (third column). All five specimens were subsequently used for generating a probabilistic AAN atlas, which provides spatial priors for the automated Bayesian segmentation of AAN nuclei in MRI images of any contrast (fourth column). Zoomed panels are provided for the midbrain histological sections (M1 and M2), and the pontine histological sections (P1 and P2), which display boundaries of each AAN nucleus.

2.5 | Probabilistic Atlas Construction and Bayesian Segmentation

2.5.1 | Ex Vivo MRI Dataset

To optimize the accuracy of segmentation, a probabilistic atlas needs to describe not only the neuroanatomical structures of interest but also their surrounding tissue. With this purpose, we ran our sequence adaptive segmentation method (SAMSEG, Puonti et al. 2016) on the low-*b* image of the ex vivo scans to obtain labels for 36 different brain structures, including the whole brainstem, left and right cerebellar gray and white matter, fourth ventricle, left and right ventral diencephalon (DC), and the left and right thalamus. After manual correction of errors made by SAMSEG, the manual segmentations of the arousal nuclei were overlaid on these automated segmentations to create composite label maps including both the brainstem nuclei of interest and surrounding structures. These composite maps were used to create the probabilistic atlas using a Bayesian technique, as described in Section 2.5.2 below and illustrated in Figure 2. A fly-through visualization of the atlas mesh is provided in Video S1, which can be accessed through [Zenodo](#).

2.5.2 | Generative Model of Segmentations and Atlas Construction

The Bayesian segmentation framework relies on a generative model of brain MRI data, where neuroanatomy and model

formation are decoupled (Ashburner and Friston 2005; Van Leemput et al. 1999). This approach enables the use of ex vivo data of superior quality to model neuroanatomy through a probabilistic atlas, and the application of the atlas to automated segmentation of in vivo scans or arbitrary MR contrast.

The generative model of Bayesian segmentation assumes that segmentations are generated by a probabilistic atlas. Here we used the representation proposed by (Van Leemput 2009), where a probabilistic atlas is encoded as a tetrahedral mesh endowed with a deformation model. Every mesh node has an associated vector with the probabilities of the different neuroanatomical classes happening at each location, and such probabilities can be evaluated at any other location with interpolation. The forward model is as follows: if \mathbf{x}^r is reference position of the mesh nodes, a deformed position \mathbf{x} is first obtained from the probability distribution:

$$p(\mathbf{x} | \mathbf{x}^r, \mathbf{K}, \gamma) \propto \exp \left[-\gamma \sum_t U_t^{\mathbf{K}}(\mathbf{x}, \mathbf{x}^r) \right]$$

where γ is a scalar representing the stiffness of the deforming mesh, \mathbf{K} is the connectivity (topology) of the mesh, and $U_t^{\mathbf{K}}$ is a potential function that penalizes the deformation of the t -th tetrahedron, going to infinity as the Jacobian determinant goes to zero (if the tetrahedron folds onto itself), and thus preserving the topology of the mesh (Ashburner et al. 2000). Given the deformed mesh, and the label probabilities at each node $\alpha = \{\alpha_i\}$, the probability of observing class k at a certain voxel location j is obtained with barycentric interpolation:

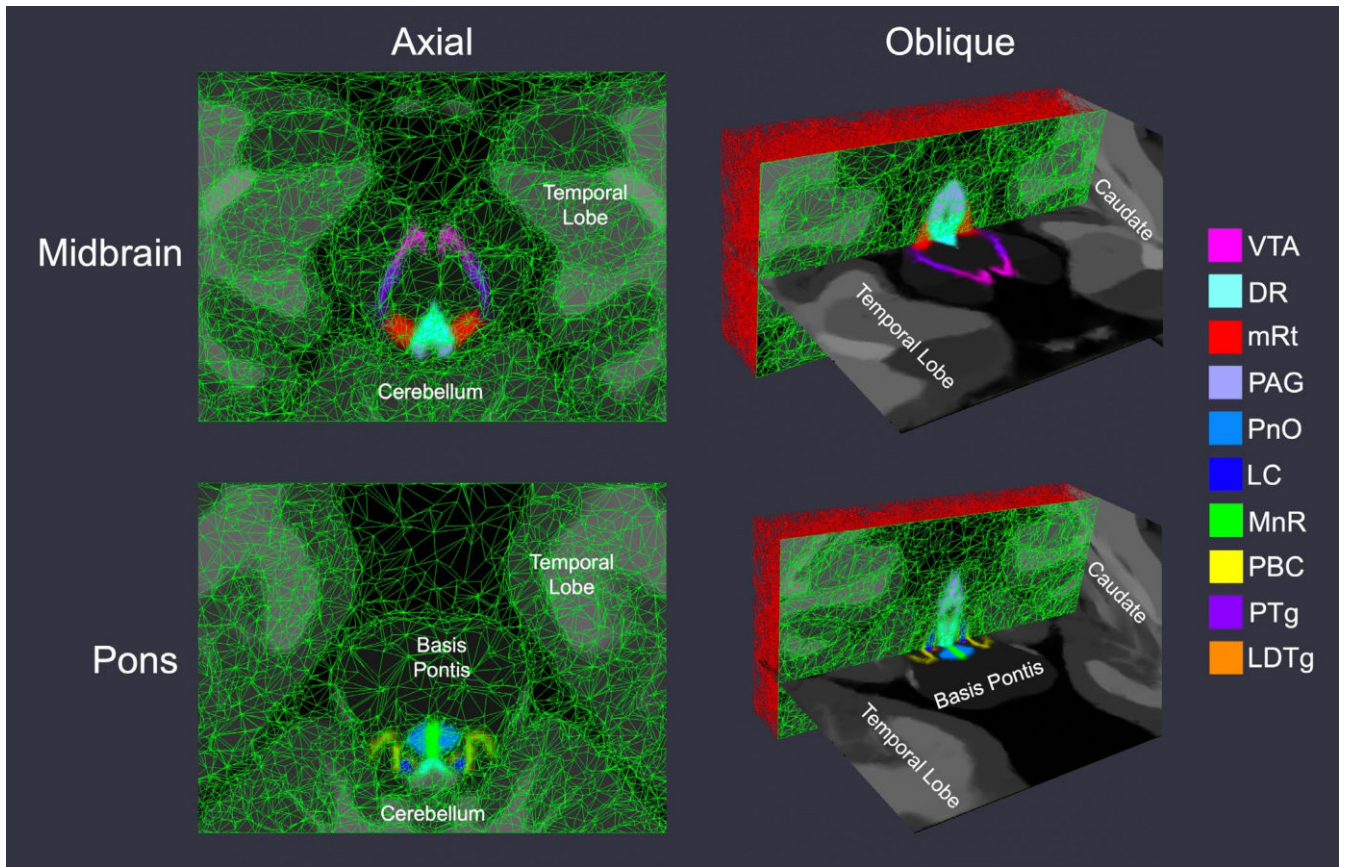


FIGURE 2 | Probabilistic atlas mesh of ascending arousal network nuclei. We show axial and oblique views (with coronal mesh sections) of the adaptive probabilistic atlas mesh used to encode spatial priors for all nuclei in the midbrain (top row) and pons (bottom row). Mesh node density corresponds to the relative amount of intensity information used for atlas construction and subsequent Bayesian segmentation. All SAMSEG-derived brain structures (including the whole brainstem) used for atlas construction are displayed with gray intensities.

$$p_i(k | \alpha, \mathbf{x}, \mathcal{K}) = \sum_n \alpha_n^k \phi_n(\mathbf{r}_j)$$

where \mathbf{r}_j is the spatial location of node n and ϕ_n is an interpolation basis function attached to it. The generative model of segmentations is completed by assuming that a segmentation or label map L is obtained by sampling these label probabilities independently at each voxel location:

$$p(L | \alpha, \mathbf{x}, \mathcal{K}) = \prod_j p(L_j | \alpha, \mathbf{x}, \mathcal{K})$$

Building the atlas requires “inverting” the model with Bayesian inference, in order to estimate its parameters (reference position, label probabilities and topology) from a set of M example segmentations $\{L_m\}_{m=1}^M$. Assuming no prior knowledge on the distribution of these parameters, the problem to solve is:

$$\begin{aligned} \{\hat{\alpha}, \hat{\mathbf{x}}, \hat{\mathcal{K}}, \hat{\gamma}\} &= \operatorname{argmax}_{\{\alpha, \mathbf{x}^r, \mathcal{C}, \gamma\}} p(\alpha, \mathbf{x}^r, \mathcal{K}, \gamma | \{L_m\}) \\ &= \operatorname{argmax}_{\{\alpha, \mathbf{x}^r, \mathcal{C}, \gamma\}} p(\{L_m\} | \alpha, \mathbf{x}^r, \mathcal{K}, \gamma) \end{aligned}$$

This maximization is difficult because of the need to optimize for the connectivity \mathcal{K} , which is a Bayesian model selection problem. We use a “greedy algorithm” that starts from a very dense mesh and slowly merges tetrahedra where appropriate, using

Bayesian model selection. Further details can be found in (Van Leemput 2009).

2.5.3 | Segmentation as Bayesian Inference

The full generative model of Bayesian segmentation combines two components: the prior and the likelihood. The prior describes the distribution of segmentations $p(L | \alpha, \mathbf{x}^r, \mathcal{K}, \gamma)$, as described in Section 2.5.2 above. The likelihood describes the distribution of observed image intensities given a segmentation L . Here we follow the classical model of Bayesian segmentation and assume that: (i) each class k has an associated Gaussian distribution with mean μ_k and variance σ_k^2 ; and (ii) the intensity of voxel j is an independent sample of the Gaussian distribution associated with its label L_j . Therefore:

$$p(I | L, \{\mu_k\}, \{\sigma_k^2\}) = \prod_j p(I_j | \mu_{L_j}, \sigma_{L_j}^2)$$

where I represents the observed image intensities, and $p(I_j | \mu_{L_j}, \sigma_{L_j}^2)$ is simply the Gaussian distribution $\mathcal{N}(I_j; \mu_{L_j}, \sigma_{L_j}^2)$.

Using Bayesian inference, segmentation within this model can be posed as the following optimization problem:

$$\hat{L} = \operatorname{argmax}_L p(L | I, \alpha, \mathbf{x}^r, \mathcal{K}, \gamma)$$

However, this requires marginalizing over model parameters, including the mesh deformation \mathbf{x} , which is intractable. Instead, the standard approximation is to compute point estimates for the parameters, and then solve the segmentation. The objective function to optimize is:

$$\{\hat{\mathbf{x}}, \{\hat{\mu}_k, \hat{\sigma}_k^2\}\} = \operatorname{argmax}_{\{\mathbf{x}, \{\mu_k, \sigma_k^2\}\}} p(\mathbf{x}, \{\mu_k, \sigma_k^2\} | \mathbf{I}, \boldsymbol{\alpha}, \mathbf{x}^r, \mathcal{K}, \gamma)$$

$$\operatorname{argmax}_{\{\mathbf{x}, \{\mu_k, \sigma_k^2\}\}} p(\mathbf{x} | \mathbf{x}^r, \mathcal{K}, \gamma) p(\{\mu_k, \sigma_k^2\}) \sum_L p(\mathbf{I} | \mathbf{L}, \{\mu_k, \sigma_k^2\}) p(\mathbf{L} | \boldsymbol{\alpha}, \mathbf{x}, \mathcal{K})$$

where $p(\{\mu_k, \sigma_k^2\})$ encodes prior knowledge on the Gaussian parameters, if available. Optimization is performed with a coordinate ascent strategy, alternately maximizing for the atlas deformation \mathbf{x} (with the L-BFGS algorithm, (Byrd et al. 1995)) and the Gaussian parameters $\{\mu_k, \sigma_k^2\}$ (with the Expectation Maximization algorithm (Dempster et al. 1977)). It is straightforward to show that the final segmentation, as well as the expectation of volumes of the different structures, are obtained as a byproduct of the EM algorithm. Further details can be found in (Van Leemput 2009).

2.5.4 | Implementation of the Segmentation Method

Because linear deformation aspects were not considered in the generative model, external affine alignment is required both for atlas building and segmentation. In atlas building, we align a binary mask consisting of the whole brainstem (including arousal nuclei), left and right ventral DC, and thalami to the corresponding grouping of structures in the FreeSurfer atlas and consider only a cuboid enclosing the mask with a margin of 15 mm. In segmentation, we assume that the scan to segment has been run through the main FreeSurfer stream. Then, we can similarly co-register the same subset of structures in the FreeSurfer atlas with a binary mask including the thalami, ventral DC, and brainstem, as automatically estimated by FreeSurfer.

A crucial aspect for segmentation robustness is to group structures with similar intensity profiles into superclasses. Therefore, all gray matter structures in the cerebrum (cerebral cortex, hippocampus, amygdala) share a single set of Gaussian parameters, as do cerebrospinal fluid (CSF) regions (lateral, third, and fourth ventricles) and brainstem structures (brainstem, ventral DC and arousal nuclei except for the PAG, which displays some contrast and has its own Gaussian distribution). The rest of the structures in the atlas have their own sets of Gaussian parameters, including the caudate nucleus, accumbens area, putamen, pallidum, thalamus, choroid plexus, cerebral white matter, cerebellar white matter, cerebellar cortex, and background.

At segmentation, we also exploit the output of the main FreeSurfer stream in two ways. First, we use the coarse skull stripping provided by FreeSurfer to remove most of the extra-cerebral tissue. Second, we use the automated segmentation (ASEG) to inform the Gaussian parameters for each superclass (except for the PAG) as with the median intensity of the voxels within each segment using a conjugate prior. Further details can be found in (Iglesias, Van Leemput, et al. 2015).

2.5.5 | Evaluation Details

We utilized Dice scores and 95th-percentile Hausdorff distances (HD) for evaluating segmentation accuracy as compared to manual labeling for all AAN nuclei. For two binary masks M_a and M_b , Dice coefficients and HDs are defined as:

$$\text{Dice}(M_a, M_b) = \frac{2 \cdot |M_a \cap M_b|}{|M_a| + |M_b|}$$

$$\text{HD}(M_a, M_b) = \max \left\{ q_{95} \left(\left\{ \inf_{b \in M_b} \{d(a, b)\} \mid a \in M_a \right\} \right), q_{95} \left(\left\{ \inf_{a \in M_a} \{d(b, a)\} \mid b \in M_b \right\} \right) \right\}$$

where $|\cdot|$ represents the cardinality (volume) of a region, $d(\cdot, \cdot)$ represents Euclidean distance and $q_{95}(\{\cdot\})$ represents the 95th percentile (quantile) value of a set. We chose to evaluate accuracy with both Dice score and HD because of the relatively small size of the nuclei. Dice scores, which are mainly a volume-specific measure, tend to be highly variable with small shifts between compared regions. In contrast, HD is a boundary metric that is less impacted by the relative sizes of compared regions and thus provides a more robust measure of overall alignment between manual annotations and automated segmentations.

3 | Results

3.1 | Segmentation Accuracy for In Vivo T1 Scans From Control and TBI Subjects

Figure 3 shows the Dice coefficients and corresponding HDs for the 10 control subjects and 10 deformed/lesioned brainstems from patients with severe TBI. As expected, Bayesian segmentations of nuclei with thin cross-sectional areas, mainly the LC (Dice: 0.38), LDTg (Dice: 0.18), and PBC (Dice: 0.19), displayed the lowest degrees of direct overlap with manual annotations in control subjects. The rest of the AAN nuclei displayed consistently better overlap with mean Dice coefficients over 0.5. Although such degrees of overlap are low for standard segmentation algorithms, this is expected given that AAN nuclei are orders of magnitude smaller than most regions in the brain that are segmented by standard algorithms. HD, a distance metric that captures boundary precision and is less sensitive to small changes in overlap (as compared to Dice coefficients), was less than 2 mm for all AAN nuclei except for the PBC in control subjects (HD: 2.17 mm), reflecting the high precision of the algorithm. Minimal alteration in Dice coefficients and HD was observed for the 10 TBI patients, with only slight decreases in segmentation accuracy and precision. This observation indicates that the Bayesian segmentation algorithm is, to a degree, robust to lesioning and deformation in the brainstem.

An example of AAN segmentations adapting to the patterns of tissue injury observed in TBI, which distort the local anatomy of AAN nuclei, is illustrated in Figure 4. Although the algorithm adapts well to tissue deformation and small lesions, we observed poorer performance with larger brainstem lesions, where the algorithm erroneously “inpainted” (i.e., filled in voxels not belonging to a segmented region with the segmentation label) the lesions with labels of proximal nuclei, such as in Figure 5. Representative

slices for manual annotations and Bayesian segmentations for each control and TBI subject are illustrated in Figure S4.

Finally, we synthetically downsampled the T1 MRI scans from the control subjects and TBI patients via Gaussian blurring and re-gridding via a kernel with a standard deviation set to mimic isotropic resolutions between the native resolution (1 mm) and 3.5 mm with 0.25 mm increments (Figure 6). This synthetic resampling showed that segmentation of each nucleus, including to an extent small nuclei such as the LC, LDTg, and PBC, retained spatial accuracy comparable to the 1 mm resolution accuracies down to isotropic resolutions of 2–2.5 mm.

3.2 | Test–Retest Analysis

We performed test–retest analysis for two different structural sequences to evaluate the algorithm’s consistency and reproducibility

in segmentation of the same anatomy under varying scanning conditions. We observed robust test–retest reliability for both T1 and T2 MRI scans of subjects from the HCP “retest” dataset (Figure 7). Intraclass correlation coefficients (ICCs) are expected to be low for segmentations of small regions that are prone to fluctuations of estimated volume, but we observed excellent reliability (ICC > 0.75) for all AAN segmentations except for the right LC and right LDTg for analysis in the same domain (i.e., T1–T1 and T2–T2). We also observed ICC > 0.7 across domains (i.e., T1–T2 and T2–T1), with exceptions for the DR, PAG, LC and LDTg. While there was a small drop-off in ICC with decreasing segmentation volume, as shown in the volume-versus-ICC scatter plot (Figure 7A), this relationship was not statistically significant based on a Wald *t*-test for deviation from a zero-slope null hypothesis ($R = 0.26$, $p = 0.33$). This result indicates that Bayesian AAN segmentation reliability does not significantly decline with the spatial volume of the AAN nucleus. Furthermore, the drop-off in reliability estimates for the cross-domain experiments, especially for small nuclei such as the LC,

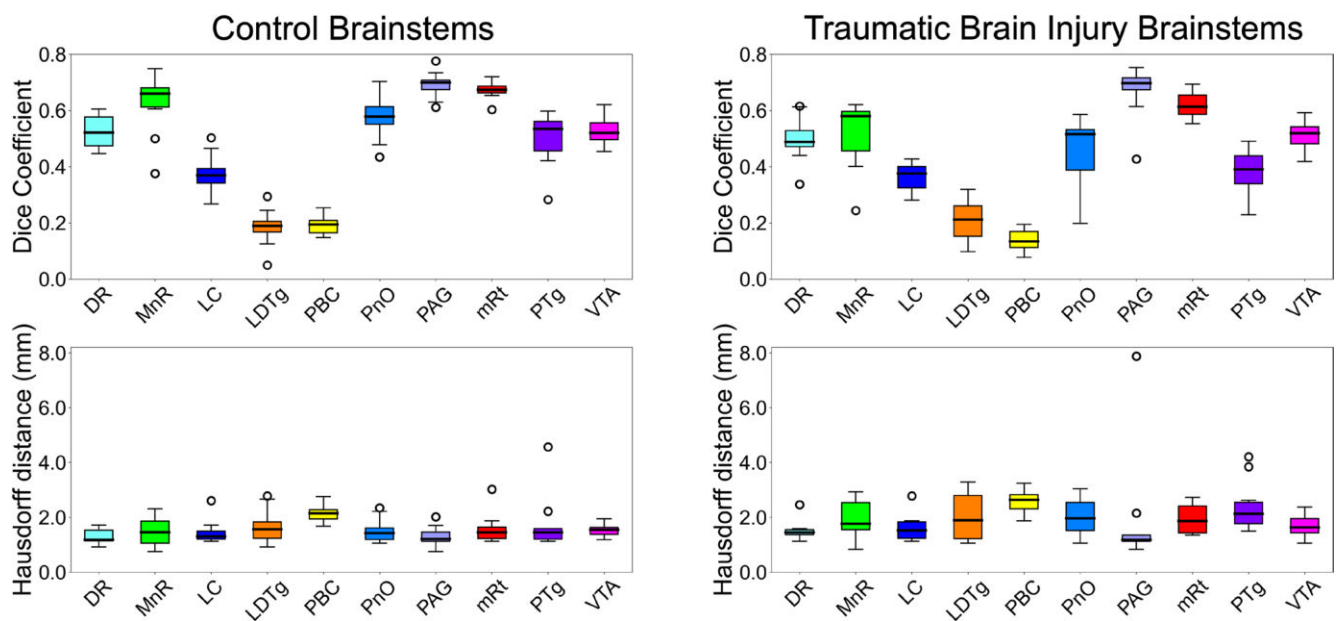


FIGURE 3 | Bayesian segmentation accuracy in control and TBI T1 MRI scans. Displayed in the left panel are box plots of Dice coefficients (top) and associated 95% Hausdorff distances (HD, bottom) from direct comparisons of automated segmentations and manual annotations of each AAN nucleus in 10 T1 MRI scans from healthy control subjects. Shown in the right panel are Dice scores (top) and HD (bottom) derived from 10 TBI patients with deformed and/or lesioned brainstems. Divisions of the box plots are the 25th percentile, median, and 75th percentile.

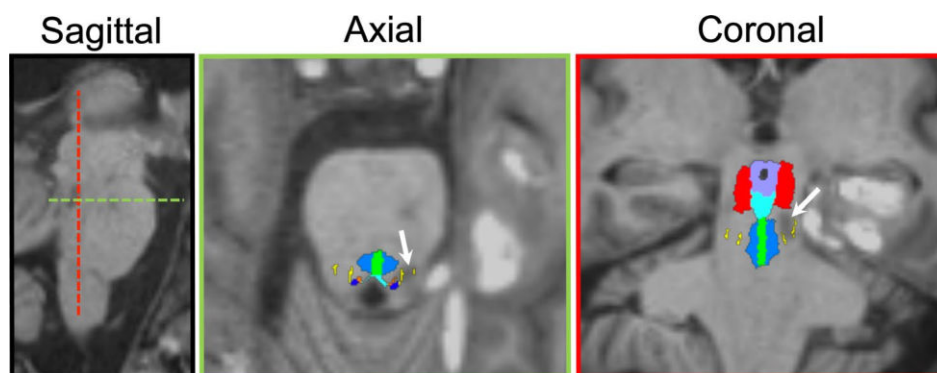


FIGURE 4 | Bayesian segmentation of AAN nuclei in a T1 scan of a TBI patient’s brainstem that is laterally deformed by a large medial temporal-lobe lesion. The brainstem also contains a hypointense hemorrhagic lesion in the pontine tegmentum, which is flanked by the parabrachial complex. The white arrows in each panel point to the location of the brainstem lesion, which was confirmed with susceptibility-weighted imaging.

LDTg and PBC, suggests that segmentation is driven by MR contrast more than by global propagation of probabilistic atlas information (e.g., through the registration step) for HCP-quality scans.

3.3 | Classification Performance in AD

To demonstrate the clinical translatability of Bayesian AAN segmentation in group studies, and specifically its ability to

classify individuals with neurodegenerative disease, we assessed changes in spatial volume of each AAN nucleus in T1 MRI scans between healthy and AD subjects from the ADNI dataset. Significant decreases in the volume of the whole brainstem, particularly rostral midbrain volumes, have been reported in individuals with AD (Lee et al. 2015). To our knowledge, no volumetric analysis has been performed on AAN nuclei, even though histologic alterations in several AAN nuclei, including the LC and the raphe nuclei, have

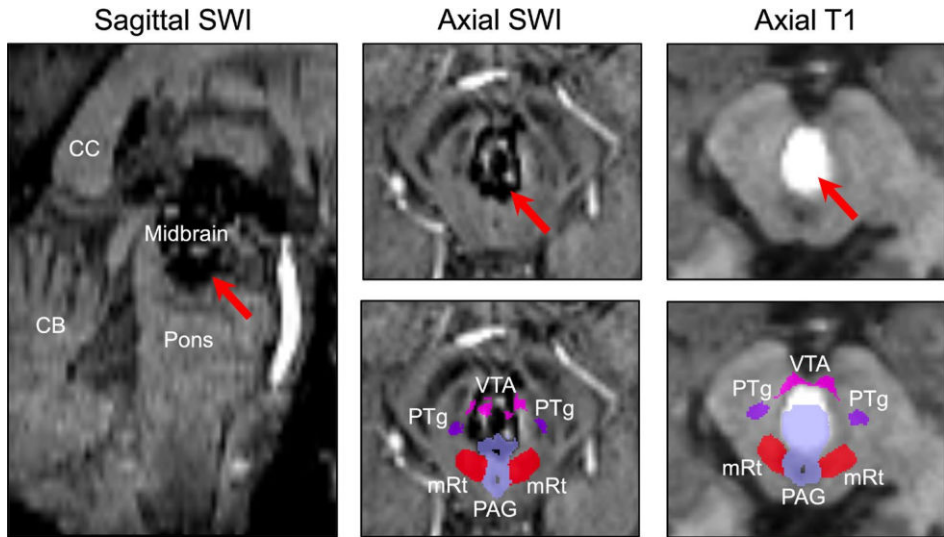


FIGURE 5 | Inpainting of AAN segmentations in the presence of a large brainstem lesion. MRI scanning of patient 15 (see [Supporting Information: Tables](#)) revealed a large hemorrhagic lesion spanning the entire rostro-caudal axis of the midbrain, as seen in the sagittal view (left), bordering the PAG, mRt, PTg, and VTA. The lesion is hypointense in SWI and hyperintense in T1, as indicated by the red arrows (top axial panels). Automated segmentation of AAN nuclei in both the SWI and the T1 images yielded significant overlap of the PAG label, and to a lesser degree the VTA label, inside of the lesion margins (bottom axial panels).

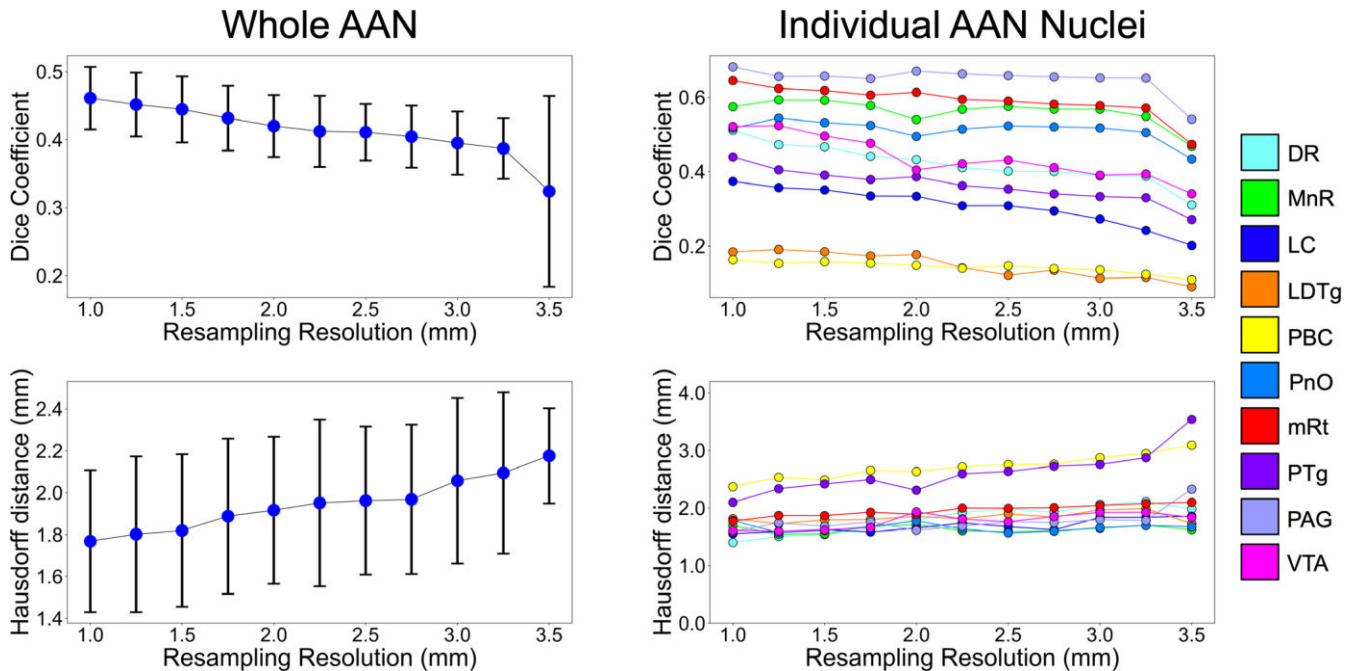


FIGURE 6 | Bayesian segmentation accuracy in synthetically resampled T1 MRI scans. Displayed in the left panels are Dice coefficients (top) and HDs (bottom) with corresponding standard deviation bars across all AAN nuclei in the 20 (10 control and 10 TBI) subjects with manual AAN annotations for varying degrees of spatial resampling. Resampling was performed from the native 1-mm isotropic resolution to 3.5-mm resolutions. The right column displays Dice coefficients (top) and HDs (bottom) for each individual AAN nucleus averaged across all subjects for the same synthetic resolution span.

been implicated in AD progression (Chen et al. 2022; Simic et al. 2009).

For our volume classification model, we implemented a linear discriminant analysis (LDA) classifier, due to its linearity and simplicity (Figure 8). This allows for the underlying volumes of AAN nuclei to more directly affect discriminatory performance, as opposed to the explicit parameterization of the classifier. We trained the LDA classifier with the volume of each segmented AAN nucleus as a separate feature with leave-one-out cross-validation. For classification analysis, we constructed a receiver-operating characteristic (ROC) curve by varying the threshold of the LDA likelihood ratio. We also implemented corresponding ROC curves by varying the classification threshold for the volumes of the entire masked AAN, as well as the whole brainstem extracted from the FreeSurfer *aseg* package. For statistical comparison, we calculated areas under the curve (AUCs) for each classifier, as well as paired DeLong tests (DeLong et al. 1988) between pairs of classifiers.

Classification performance based on the respective ROC curves was comparably poor for the brainstem and whole-AAN masks with AUCs of 0.58 and 0.57, respectively. Conversely, the LDA classifier built on individual AAN nuclei outperformed both whole-brainstem and whole-AAN classification, with an AUC

of 0.75 and a DeLong $p < 0.001$ for comparisons with both of the aforementioned classifiers. This significant boost in power of the LDA classifier is most likely attributable to the individual classification power of a large subset of the AAN nuclei. Eight out of the 16 nuclei (excluding their left-right subdivisions) showed volume reduction in the AD cohort that was statistically significant with Bonferroni correction (Table 3). Notably, all of the AAN nuclei with significant volume reduction have previously been shown to exhibit morphological and/or histological alterations in individuals with AD (Mufson et al. 1988; Parvizi et al. 1998, 2000, 2001).

3.4 | Correlations With Susceptibility-Weighted Imaging in Patients With Severe TBI

To display the robustness of the algorithm to detecting changes in imaging markers consistent with structural pathology in the brain, we showed correlations between SWI intensities in AAN masks and behavioral metrics in TBI patients. Specifically, we analyzed SWI scans in 15 of the 18 patients from the TBI dataset (see protocol in Section 2.2.3) to assess the correlation between the degree of structural AAN injury and functional measures of consciousness and clinical outcomes. Three SWI scans were excluded from analysis due to the presence of motion artifacts. We used SWI because this sequence is sensitive to and creates particularly high contrast in hemorrhagic lesions commonly observed in TBI (Bianciardi et al. 2021; Tao et al. 2015). Representative slices from all SWI scans are illustrated in Figure S5.

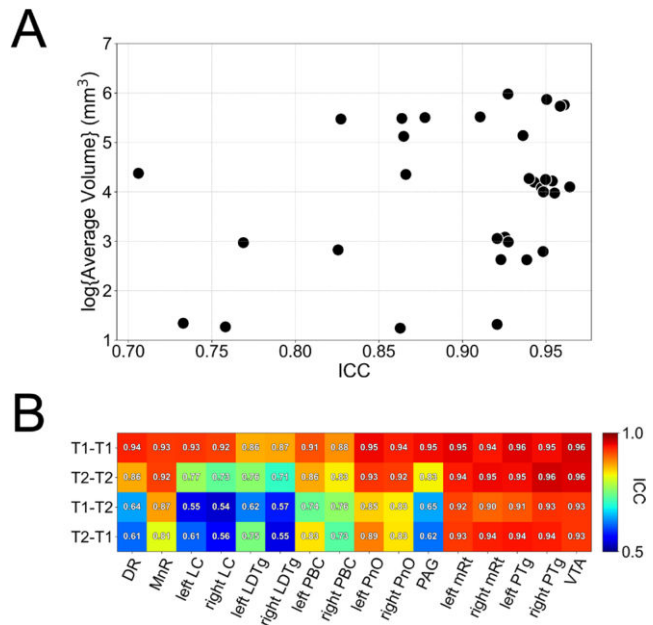


FIGURE 7 | Test-retest analysis for volumes of segmented AAN nuclei. Shown in Panel (A) are the spatial volumes in log-space of segmented AAN nuclei compared to their respective ICC values for T1-T1 and T2-T2 comparisons. Each scatter point corresponds to the log of the average volume of each nucleus calculated between all subjects and scanning sessions (i.e., for both the “test” and the “retest” scans). T1 and T2-segmented nucleus volumes are shown as separate scatter points. Shown in panel (B) are the ICC values, along with a corresponding heat map, for each segmented AAN nucleus for test-retest analysis between two MR contrasts: T1 in the test set and T1 in the retest set (T1-T1), T2 in the test set and T2 in the retest set (T2-T2), T1 in the test set and T2 in the retest set (T1-T2), and T2 in the test set and T1 in the retest set (T2-T1).

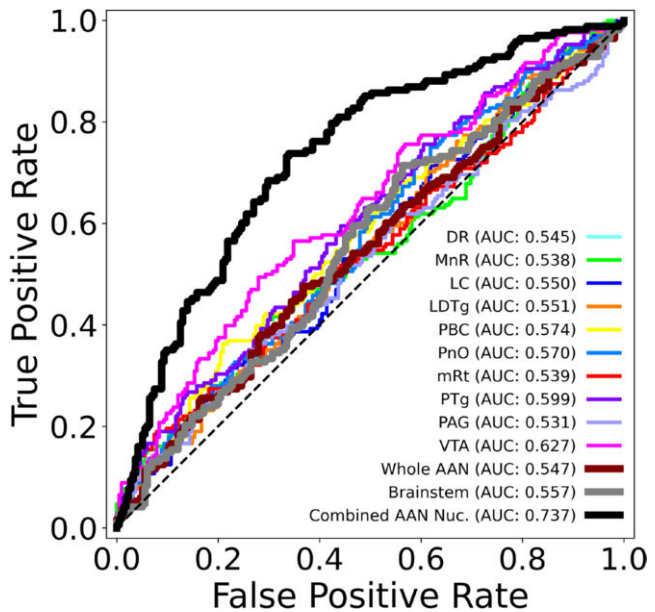


FIGURE 8 | ROC analysis of AAN segmentations in Alzheimer's disease. Displayed are ROC curves for a classification task (between healthy control and AD subjects in the ADNI dataset) based on a varying threshold for the volumes of a brainstem mask (gray), the segmented whole-AAN mask (maroon), the likelihood ratio of a multi-feature LDA classifier trained on combined segmented AAN nuclei (black), as well as one- or two-feature LDA each individual AAN nucleus. For individual (non-midline) AAN nuclei with left-right subdivisions, each subdivision was incorporated as a separate LDA classifier feature.

Each SWI image was first normalized by the spatially averaged SWI intensity within the lateral ventricles. The lateral ventricles for each patient were segmented using the FreeSurfer SynthSeg tool and then manually corrected to remove hypointense regions of hemorrhage in the CSF. Normalized SWI intensities, calculated per voxel as the ratio of the raw SWI signal to the spatially averaged ventricular SWI signal, were used to standardize SWI signal across individual scans. We then calculated the spatial average of these normalized SWI intensities inside the union of all 10 (including left–right subfields) segmented AAN nuclei (referred to as the “whole-AAN mask”). Finally, we compared the averaged normalized whole-AAN SWI signal to two metrics that were used to assess the patient’s level of consciousness (LoC) at the time of scanning: the total GCS (GCS) score and the total Coma Recovery Scale-Revised (CRS-R) score (Giacino et al. 2004). Assessment of both LoC metrics yielded strong positive correlations ($R = 0.65$ and 0.60 for GCS and CRS-R, respectively) (Figure 9). Both correlations were statistically significant based on a zero-slope null hypothesis ($p = 0.008$ and 0.018 for GCS and CRS-R correlations, respectively).

4 | Discussion

Historically, a major barrier to advancing knowledge about the brainstem’s role in the physiology of human consciousness and the pathophysiology of DoC has been the lack of tools for identifying and segmenting the tiny gray matter nuclei of the brainstem’s AAN. Here, we develop and disseminate an automated segmentation tool and a probabilistic atlas of 10 AAN nuclei built from immunostaining data and meticulous manual segmentation of AAN nuclei in five ultra-high-resolution ex vivo MRI datasets. The AAN atlas generation process is built on a Bayesian framework, which can segment AAN nuclei in any MRI modality. We validated this tool with comparisons to in vivo manual annotations, as well as assessment of test–retest reliability. Further, we demonstrate the clinical translatability of the method by detecting volumetric changes of AAN nuclei in patients with AD, and by correlating

AAN SWI intensities with behavioral measures of consciousness in patients with severe TBI.

The Bayesian AAN segmentation tool developed here builds upon recent efforts by progressing from segmentation of medullary, pontine, and midbrain subregions (Iglesias, Van Leemput, et al. 2015) to segmentation of individual AAN nuclei. The core of the segmentation method is the probabilistic atlas mesh, which was constructed from five ex vivo human brain specimens. Both the accuracy and the spatial variation of the atlas mesh depend on the manual annotation of each AAN nucleus, which was performed directly on low-b images with direct reference to corresponding $200\text{ }\mu\text{m}$ FLASH images in all ex vivo brain specimens, along with corresponding histological sections in two of the five specimens. Although access to histology is preferable for the delineation of contrast boundaries of small AAN nuclei, we have empirically found that FLASH contrast is sufficient for proper delineation of these nuclear borders. We observed corresponding contrast boundaries between histology and FLASH space in seven of the 10 AAN nuclei, which provide adjacent locations for delineation of the remaining nuclei, as visualized in Figure S1. This correspondence between histological and high-resolution MRI contrast within ex vivo brainstems is corroborated by prior studies (Agostinelli et al. 2023; Donatelli et al. 2023). With further quantification of error between ground-truth histology and high-resolution ex vivo MRI, we anticipate that future iterations of probabilistic atlases and companion brainstem segmentation methods may be able to rely on MRI contrast alone.

We demonstrate the accuracy of the AAN segmentation tool in manually traced in vivo T1 data with guidance from a brainstem atlas. This manually traced dataset consisted of a 10-subject control dataset as well as a 10-patient TBI dataset where brainstems were either lesioned or deformed due to hemorrhagic and/or edematous intracranial lesions. Dice coefficients for larger AAN nuclei were all greater than 0.5 . Although modest compared to previously published Dice coefficients for segmentations of larger brain structures (Fischl et al. 2002; Iglesias, Van Leemput, et al. 2015; Wasserthal et al. 2018), the reported AAN Dice coefficients are expected given the relatively small size of AAN nuclei. This challenge is especially relevant to the smaller nuclei (e.g., LC, LDTg, and PBC), whose cross-sections can be as thin as one voxel in certain regions (in terms of the 0.4 mm Bayesian segmentation volumes). Our reported AAN Dice coefficients and HDs are comparable to algorithms that segment small brain regions with volumes that are similar to those of AAN nuclei, such as hypothalamic and thalamic nuclei (Billot et al. 2020; Tregidgo et al. 2023). Notably, there was less variability in HDs (a metric that is largely invariant to ROI size) between segmentations of AAN nuclei and their corresponding manual annotations, with all average distances being below 2.5 mm . These low HDs imply that our automated segmentations retain spatial specificity for all AAN nuclei regardless of size.

The robustness of the Bayesian AAN segmentation tool is further demonstrated by the test–retest reliability analyses. We compared the spatial volumes of segmented AAN nuclei in T1 and T2 sequences of HCP subjects who underwent two separate scanning sessions. Test–retest ICC scores for AAN volumes derived from the same sequence (T1–T1 and T2–T2) were all

TABLE 3 | Shown are the segmented AAN nuclei that displayed a statistically significant reduction in volume in the AD cohort compared to healthy controls based on a Bonferroni-corrected ($n = 16$) two-tailed Wilcoxon rank–sum test.

AAN nucleus	p	ROC AUC	Δ volume (mm^3)
VTA	<0.001	0.627	-18.1
Left PTg	<0.001	0.606	-3.4
Right PTg	<0.01	0.606	-3.7
Left PBC	<0.01	0.576	-1.5
Right PBC	<0.01	0.583	-1.7
PAG	<0.01	0.531	-10.7
Left PnO	<0.05	0.556	-2.4
Right PnO	<0.05	0.543	-2.0

Note: The third column displays the net reduction in cohort-averaged volumes for each AAN nucleus.

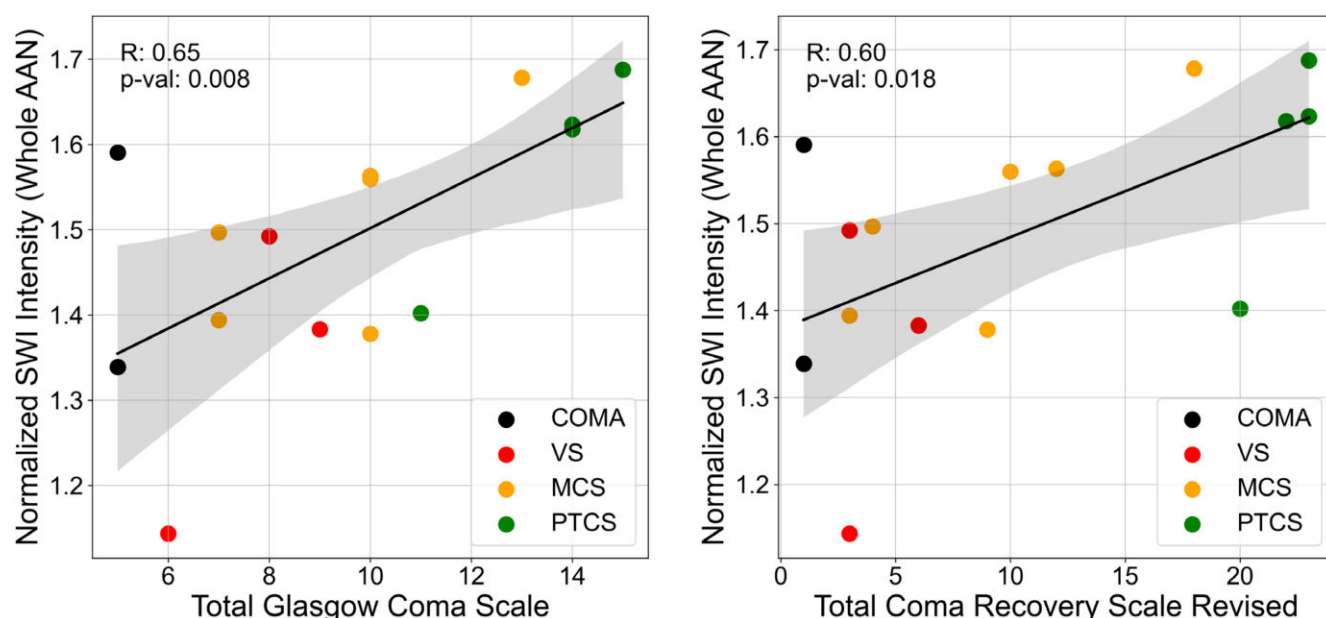


FIGURE 9 | SWI AAN correlations with LoC. The average SWI intensity was calculated within the union of all 10 segmented AAN nuclei and normalized by the average SWI intensity within the lateral ventricles for each TBI patient scan. This normalized AAN SWI value was calculated for 15 patients with acute TBI and correlated with their assigned LoC assessments: the total GCS score (left panel), and the total CRS-R score (right panel). Coloring of the scatter points indicates each TBI patient's LoC classification: coma; VS, vegetative state; MCS, minimally conscious state; PTCS, post-traumatic confusional state. R values are derived from a linear least-squares regression, and p values indicate the significance of deviation of the regression lines from a zero-slope based on a two-tailed Wald t -test.

greater than 0.8, with the exception of the LC and LDTg. Test-retest ICC scores for AAN nuclei volumes derived from alternating sequences (T1–T2, and T2–T1) were greater than 0.7, with the exception of the LC, LDTg, DR, and PAG. For the majority of AAN nuclei, the high repeatability of volume measurement indicates that segmentations are leveraging actual MR contrast as opposed to noise. Notably, each of the nuclei with low ICCs (LC, LDTg, DR, and PAG) is positioned proximal to tissue–CSF boundaries, which are prone to high noise levels. Brainstem–CSF boundaries, especially the dorsal brainstem—fourth ventricle border, have lower signal-to-noise ratios due to both partial-volume averaging and CSF pulsatility effects, which have been observed in dorsal brainstem nuclei such as the PAG and DR (Sclocco et al. 2018). These results suggest that further optimization of the segmentation tool is needed in future studies and that analyses of AAN nuclei located at brainstem–CSF boundaries should be interpreted with caution.

We performed proof-of-principle analyses of the segmentation of AAN nuclei in patients with AD and severe TBI to demonstrate the clinical utility of the algorithm in disease classification and correlation tasks. For AD analysis, our goal was to assess the utility of the algorithm as a disease-detection tool through its robustness in classifying subjects into either healthy control or AD categories solely with biomarkers detected through automated segmentation. In patients with AD, the segmentation tool detected differences in AAN volumes, as compared to healthy controls. Neuropathologic changes in AAN nuclei have been reported in pathology studies of patients with AD (Rüb et al. 2016; Uematsu et al. 2018) but MRI studies of changes in the AAN are scarce (Galgani et al. 2023; Miyoshi et al. 2013; Takahashi et al. 2015), likely due to the difficulty of manual and automated AAN segmentation.

Whereas classification of volumetric differences was similar for the brainstem and whole-AAN masks, there was a significant boost in classification performance for the LDA classifier trained on individual AAN nuclei, with an AUC increase of 0.18 (LDA classifier versus whole-AAN mask). In each AAN nucleus with a statistically significant change in volume, we observed a reduction in volume in the AD patient group. This volume loss is consistent with prior MRI studies, which reported volumetric reduction in the midbrain and pontine tegmentum where most AAN nuclei are located (Ji et al. 2020; Lee et al. 2015). The VTA, which contains dopaminergic neurons that widely project to and modulate numerous cortical regions (Morales and Margolis 2017), displayed the most significant volumetric decrease in patients with AD. This observation is supported by previous imaging and neuropathology studies, which found that AD progression correlates with volume loss and dopamine neuron degeneration in the VTA (Bozzali et al. 2016, 2019; Gibb et al. 1989; De Marco and Venneri 2018). In our AD analysis, we note the potential limitation that all subjects within the AD subgroup were classified based on purely behavioral criteria. Additional confirmatory biomarkers for AD, such as amyloid positivity status with C^{11} -PIB positron emission tomography, were only performed on a small subset of AD subjects in ADNI ($n = 24$). Possible misgrouping of subjects into the AD cohort may attenuate or distort group differences in brainstem or AAN nucleus volumes, thereby biasing the ROC curves. Our results therefore reflect classification of a behavioral phenotype rather than a biomarker-based definition of AD and should be interpreted accordingly.

Finally, we provide evidence for the utility of Bayesian AAN segmentation in an SWI-based analysis of patients with severe TBI. Specifically, we applied the segmentation method to SWI

scans and replicated prior observations that structural injury to AAN nuclei correlates with levels of consciousness and functional measures of recovery (Bianciardi et al. 2021; Edlow et al. 2013; Parvizi and Damasio 2003; Snider et al. 2019; Snider, Bodien, et al. 2020). As an indirect measure of structural injury, we show an association between the severity of hemorrhagic lesioning detected by SWI within the AAN and the LoC of each patient. Brainstem microhemorrhages detected by SWI, which are caused by traumatic shearing of arterioles and venules, are a hallmark finding of traumatic DoC because of their association with axonal shearing and disconnection of the neural networks that support consciousness (Edlow et al. 2013). Microhemorrhages within AAN nuclei appear to have particular prognostic relevance (Bianciardi et al. 2021; Izzy et al. 2017). We observed a correlation between the normalized average SWI intensity of the AAN mask and LoC in a cohort of acute TBI patients, such that patients with lower LoC displayed lower SWI intensities (i.e., more microhemorrhages). This association between SWI intensity and LoC was observed with two behavioral assessment scores used to evaluate LoC in clinical practice: the GCS ($R=0.65$) and the CRS-R ($R=0.60$).

Our findings in patients with severe TBI complement those of a previously published SWI analysis of this same cohort, with the key distinction that the prior analysis required laborious and time-consuming manual segmentation, whereas the present analysis utilized a rapid, robust automated segmentation tool. The prior study showed associations between the total SWI lesion volume in the AAN and the duration of unresponsiveness in TBI patients (Bianciardi et al. 2021). SWI hypointensities in Bayesian-segmented AAN nuclei show superior correlations with both GCS and CRS-R, as compared to the prior study that used manually annotated AAN nuclei. Furthermore, our method displays comparable or superior correlations with the GCS and CRS-R, as compared to previously published diffusion MRI measures of structural integrity within the AAN (Jang and Kwon 2020), thalamus, internal capsule, and corpus callosum (Zhang et al. 2017), and cortico-thalamic and cortico-cortical connections (Jang et al. 2023, 2024), as well as computed tomography measures of brainstem perfusion (Xiong et al. 2022). Our analysis thus builds upon and extends these prior results in two ways: by showing strong associations between LoC and SWI contrast in the AAN, and by demonstrating the feasibility of a fully automated approach to measurement of AAN structural injury burden in TBI.

Several limitations should be considered when interpreting the Bayesian segmentation methods, as well as the experimental results. As with other algorithms that adaptively fit mesh-based atlases to segment small brain regions (Iglesias, Augustinack, et al. 2015; Iglesias et al. 2018; Puonti et al. 2016), this method provides a spatially sparse atlas mesh encoding in two scenarios. Sparse encoding either occurs inside atlas regions where annotations from different specimens correspond well, and it takes fewer mesh elements to encode label information, or around boundaries where there is high labeling variability between specimens, resulting in more “uncertain” mesh encoding and effectively a smoothed atlas region. Coarse mesh configurations during atlas formation are therefore mainly observed for AAN nuclei with loosely defined nucleus boundaries (as evidenced

in brainstem atlases (Olszewski and Baxter 1954; Paxinos et al. 2012)), which often correspond with regions of relatively homogenous MR contrast such as the LDTg, PTg, LC, MnR, and PnO, resulting in greater labeling variability. Segmentations of these nuclei are thus more uncertain because the algorithm relies on morphologic information and shape priors from the ex vivo atlas. Additionally, for lower quality MRI scans, the intensity distributions for AAN nuclei flatten and reduce the effectiveness of Expectation Maximization in estimating model priors (i.e., mesh node positioning) and tissue likelihoods. Consequently, a greater emphasis is placed on global atlas registration, and thus morphological information for AAN nuclei is mainly derived from atlas information alone. We therefore recommend that morphologic and volumetric estimates be interpreted with caution, especially in lower resolution (i.e., in vivo) and/or noisy MR sequences.

The segmentation tool also has the potential to produce irregular AAN segmentations in highly deformed and/or lesioned brainstem regions, such as by inpainting large hyperintense hemorrhagic lesions in T1 MRI scans. This irregularity likely reflects a limitation of the probabilistic atlas design, where there is a trade-off between modeling high tissue distortion and extreme tissue intensities during atlas building but losing regularization strength for anatomically plausible atlas meshing. Furthermore, the likelihood for each tissue class in the probabilistic atlas is represented by a single Gaussian distribution, which limits the scope of model fitting in lesioned tissue. Future directions will involve incorporating distributions that better capture intensity variations in the presence of lesions and evaluating the utility of convolutional neural networks (CNNs) as an alternative AAN segmentation method for lesioned or deformed brainstems. CNNs may provide enhanced flexibility to capture disease-specific contrast patterns, which are infeasible to encode in a probabilistic atlas. Furthermore, the implementation of a CNN could improve segmentation of small AAN nuclei and modeling of partial-volume and CSF pulsatility effects, thereby enhancing the segmentation accuracy of AAN nuclei in close proximity to the fourth ventricle and cerebral aqueduct.

Additional limitations include the small sample size, restricted age distribution, and variable postmortem fixation intervals (PMI) and fixation-to-imaging durations (FID) for the ex vivo data used to fit the probabilistic atlas, as well as the use of in vivo data for comparison of Bayesian segmentations to manual labels (with only a single rater performing in vivo annotations). Although only five ex vivo specimens were used for atlas building, low sample numbers for the formation of generative models (i.e., the probabilistic AAN atlas) are common and often beneficial, as to prevent model underfitting (Ng and Jordan 2001). Indeed, we observed convergence of our AAN atlas mesh with the inclusion of 3–4 specimens, with minimal alteration in mesh configuration between atlases, as illustrated in Figure S6. This observation indicates that low sample numbers of ex vivo brain specimens are sufficient for modeling the morphology of AAN nuclei. Furthermore, the relative rarity of normative ex vivo brains without gross pathology, coupled with the time commitment necessary for brain processing, makes the formation of a high-sample number atlas model challenging. This relative rarity is also why we chose in vivo MRI data for accuracy assessment with comparison to manual annotations, recognizing

that ex vivo brain specimens with finer spatial resolutions would be more suitable. This approach allowed us to use all available ex vivo data to maximize the robustness of atlas formation, and thus segmentation as a whole. However, the restricted age distribution (50–83 years) of the brain specimens used for atlas formation limits its robustness, due to the lack of incorporation of healthy young adult brains. Prior studies have shown that there is age-related atrophy of the midbrain and alterations in relaxation properties within brainstem tissue (Canales-Rodríguez et al. 2021; Iglesias, Van Leemput, et al. 2015; Luft 1999), which could have introduced atlas registration bias and affected the estimation of tissue intensity distributions during segmentation of scans from younger individuals. In future iterations, brain specimens of a younger age would allow for a more generalized AAN atlas, or even a young adult-specific atlas, to be used for segmentation.

Furthermore, we note that two of the five ex vivo brain specimens had a past medical history of depression, which could also lead to AAN morphology that is not representative of a normative cohort for atlas construction. Prior studies have shown that depression is correlated with changes in brainstem connectivity (Song et al. 2014) as well as changes in neurotransmitter expression patterns (Wong et al. 2000) for subsets of AAN nuclei. However, we did not empirically observe significant volumetric or morphological differences in the AAN nuclei of these specimens with respect to the other brain specimens. As such, given the challenge in obtaining truly “healthy” control brain specimens for ex vivo analysis, we did not consider depression as an exclusion criterion due to its population prevalence.

We note that the PMI in our ex vivo cases ranged from <24 h to 72 h, and the FID ranges from 20 to 93 months. Prior studies suggest that T2 relaxation, which is the dominant contrast in the low-*b* atlas images, changes with respect to PMI, and both T2 relaxation and overall brain volume can vary with respect to FID (Dawe et al. 2009; Kotrotsou et al. 2014; Shepherd et al. 2009). However, volumetric changes within the brainstem have been reported to be much less pronounced than in the cerebrum (Quester and Schröder 1997). As such, we expect inherent variability in the overall contrast of AAN nuclei (an effect addressed with our contrast-adaptive segmentation method), but minimal volumetric change with respect to FID. However, there may be spatial heterogeneity in how PMI and FID affect relative contrast *between* AAN nuclei. Given that the distribution of PMIs in our ex vivo cases is too narrow and coarse, we were unable to assess its effect on the spatial volumes of each AAN nucleus. Nevertheless, we did not observe any trend in AAN nucleus volume with respect to the FID, as shown in Figure S7. Both the PMI and FID ranges likely induce variability in the core annotation process, which may manifest in the overall coarseness of the mesh that encodes the probabilistic atlas. Future iterations of the algorithm can benefit from quantification of labeling uncertainty due to nuclear contrast and morphology (e.g., through multi-rater annotation) to better understand sources of variability during atlas formation.

All manual annotations of AAN nuclei in both ex vivo and in vivo MRI data were performed by a single rater. While label annotations were confirmed by a neuropathologist (H.C.K.) and neurologist (B.L.E.) with expertise in brainstem anatomy,

single-rater annotation may have introduced bias in the assessment of segmentation performance. This limitation can be addressed in future studies with a second rater re-annotating the in vivo dataset and performing inter-rater variability analysis.

Finally, our analysis is currently limited to T1, T2, and SWI MRI scans with spatial resolutions at or smaller than 1 mm (with the exception of the 1.8 mm axial resolution of the SWI scans). Synthetic downsampling (Figure 6) indicated that the segmentation accuracy of most AAN nuclei remained stable across an isotropic resolution span of 1–2.5 mm. However, application of this algorithm to scans with resolutions coarser than 1 mm should be interpreted with caution, as Gaussian blurring only provides a limited approximation of partial voluming effects, signal-to-noise ratio properties, and point spread function properties (Robson et al. 1997) observed in true lower resolution scans. Therefore, further assessment of the generalizability of this segmentation method should be performed in other MRI domains to capture the effects of varying resolutions, noise levels, scanning artifacts, and tissue contrasts on segmentation accuracy. These domains can include lower resolution diffusion and/or functional MRI sequences, emerging ultra-low-field sequences that are used in the intensive care unit (Sheth et al. 2021), and novel sequences that enhance contrast of deep brain structures (Sclocco et al. 2018).

5 | Conclusion

We present a probabilistic atlas of brainstem arousal nuclei within the AAN, a subcortical network whose connections are believed to be critical for human consciousness (Brown et al. 2010; Edlow et al. 2021; Schiff and Plum 2000). We generated the AAN atlas from ex vivo MRI with histological guidance, which allowed for highly accurate manual delineation of nuclei with boundaries that lacked MRI contrast. This probabilistic atlas serves as a backbone for a Bayesian segmentation method that allows for automated delineation of AAN nuclei in MRI scans of any contrast. We show that the Bayesian method produces accurate AAN segmentations in both healthy and lesioned/deformed brainstems and is reliable across multiple MRI contrasts in a test–retest analysis. Furthermore, morphology and intensity information from AAN nuclei have the potential to serve as imaging-based biomarkers for AD and severe TBI. Future directions to improve the proposed AAN segmentation method will include utilizing multiple contrasts, which would be especially beneficial for nuclei with faint contrast boundaries, as well as the use of a CNN to supplement or replace Bayesian inference. We release the automated tool to advance the study of human brainstem anatomy in consciousness and its disorders.

Acknowledgments

This study was supported by the NIH National Institute of Neurological Disorders and Stroke (R21NS109627, RF1NS115268, U01NS086625, U54NS115322, R01NS128961, U24NS135561, U01NS132181, U01NS137484), NIH Director's Office (DP2HD101400), NIH National Institute of Biomedical Imaging and Bioengineering (T32EB001680), NIH National Institute of Mental Health (RF1MH123195), NIH National Institute on Aging (R01AG070988), United States Department of Defense (W81XWH2210999), European Research Council

Starting Grant (677697), Alzheimer's Research UK Interdisciplinary grant (ARUK-IRG2019A-003), MIT-Takeda Fellowship, Rappaport Foundation, James S. McDonnell Foundation, MIT/MGH Brain Arousal State Control Innovation Center (BASIC) Project, and the Chen Institute MGH Research Scholar Award. We thank Kathryn Regan and Veranex Inc. for assistance with immunostaining and histology.

Data were provided in part by the Human Connectome Project, WU-Minn Consortium (Principal Investigators: David Van Essen and Kamil Ugurbil; 1U54MH091657) funded by the 16 NIH Institutes and Centers that support the NIH Blueprint for Neuroscience Research, and by the McDonnell Center for Systems Neuroscience at Washington University.

Collection and sharing of ADNI data were performed by the Alzheimer's Disease Neuroimaging Initiative (ADNI), which is funded by the National Institute on Aging (National Institutes of Health Grant U19AG024904). The grantee organization is the Northern California Institute for Research and Education. In the past, ADNI has also received funding from the National Institute of Biomedical Imaging and Bioengineering, the Canadian Institutes of Health Research, and private sector contributions through the Foundation for the National Institutes of Health (FNIH) including generous contributions from the following: AbbVie; Alzheimer's Association; Alzheimer's Drug Discovery Foundation; Araclon Biotech; BioClinica Inc.; Biogen; Bristol-Myers Squibb Company; CereSpir Inc.; Cogstate; Eisai Inc.; Elan Pharmaceuticals Inc.; Eli Lilly and Company; EuroImmun; F. Hoffmann-La Roche Ltd. and its affiliated company Genentech Inc.; Fujirebio; GE Healthcare; IXICO Ltd.; Janssen Alzheimer Immunotherapy Research & Development LLC; Johnson & Johnson Pharmaceutical Research & Development LLC; Lumosity; Lundbeck; Merck & Co. Inc.; Meso Scale Diagnostics LLC; NeuroRx Research; Neurotrack Technologies; Novartis Pharmaceuticals Corporation; Pfizer Inc.; Piramal Imaging; Servier; Takeda Pharmaceutical Company; and Transition Therapeutics.

Data Availability Statement

Representative ex vivo data used for method generation and accuracy analysis are available in OpenNeuro at (<https://openneuro.org/datasets/ds004640/versions/1.0.4>), reference number (ds004640). Corresponding histology and immunostaining data are available at (<https://histopath.nmr.mgh.harvard.edu>). The AAN atlas mesh fly-through video is available on Zenodo (<https://zenodo.org/records/15042077>). We release the segmentation algorithm and probabilistic version of the Harvard Ascending Arousal Network Atlas through the FreeSurfer software platform. Details can be found at (<https://surfer.nmr.mgh.harvard.edu/fswiki/AANSegment>).

References

Adil, S. M., E. Calabrese, L. T. Charalambous, et al. 2021. "A High-Resolution Interactive Atlas of the Human Brainstem Using Magnetic Resonance Imaging." *NeuroImage* 237: 118135. <https://pubmed.ncbi.nlm.nih.gov/33951517>.

Agostinelli, L. J., S. C. Seaman, C. B. Saper, et al. 2023. "Human Brainstem and Cerebellum Atlas: Chemoarchitecture and Cytoarchitecture Paired to MRI." *Journal of Neuroscience* 43: 221–239.

Ashburner, J., J. L. Andersson, and K. J. Friston. 2000. "Image Registration Using a Symmetric Prior—In Three Dimensions." *Human Brain Mapping* 9: 212–225.

Ashburner, J., and K. J. Friston. 2005. "Unified Segmentation." *NeuroImage* 26: 839–851. <https://doi.org/10.1016/j.neuroimage.2005.02.018>.

Augustinack, J. C., A. J. W. van der Kouwe, M. L. Blackwell, et al. 2005. "Detection of Entorhinal Layer II Using Tesla Magnetic Resonance Imaging." *Annals of Neurology* 57: 489–494.

Beissner, F., A. Schumann, F. Brunn, D. Eisenträger, and K.-J. Bär. 2014. "Advances in Functional Magnetic Resonance Imaging of the Human

Brainstem." *NeuroImage* 86: 91–98. <https://doi.org/10.1016/j.neuroimage.2013.07.081>.

Bianciardi, M. 2021. *Brainstem Navigator*. NITRC.

Bianciardi, M., S. Izzy, B. R. Rosen, L. L. Wald, and B. L. Edlow. 2021. "Location of Subcortical Microbleeds and Recovery of Consciousness After Severe Traumatic Brain Injury." *Neurology* 97: e113–e123.

Bianciardi, M., N. Toschi, C. Eichner, et al. 2016. "In Vivo Functional Connectome of Human Brainstem Nuclei of the Ascending Arousal, Autonomic, and Motor Systems by High Spatial Resolution 7-Tesla fMRI." *Magma* 29: 451–462.

Billot, B., M. Bocchetta, E. Todd, A. V. Dalca, J. D. Rohrer, and J. E. Iglesias. 2020. "Automated Segmentation of the Hypothalamus and Associated Subunits in Brain MRI." *NeuroImage* 223: 117287.

Bodien, Y. G., C. Chatelle, and B. L. Edlow. 2017. "Functional Networks in Disorders of Consciousness." *Seminars in Neurology* 37: 485–502. <https://pubmed.ncbi.nlm.nih.gov/29207410>.

Boes, A. D., S. Prasad, H. Liu, et al. 2015. "Network Localization of Neurological Symptoms From Focal Brain Lesions." *Brain* 138: 3061–3075.

Bondiau, P.-Y., G. Malandain, S. Chanalet, et al. 2005. "Atlas-Based Automatic Segmentation of MR Images: Validation Study on the Brainstem in Radiotherapy Context." *International Journal of Radiation Oncology*Biophysics* 61: 289–298.

Bozzali, M., M. D'Amelio, and L. Serra. 2019. "Ventral Tegmental Area Disruption in Alzheimer's Disease." *Aging* 11: 1325–1326.

Bozzali, M., L. Serra, and M. Cercignani. 2016. "Quantitative MRI to Understand Alzheimer's Disease Pathophysiology." *Current Opinion in Neurology* 29: 437–444.

Brown, E. N., R. Lydic, and N. D. Schiff. 2010. "General Anesthesia, Sleep, and Coma." *New England Journal of Medicine* 363: 2638–2650.

Buckner, R. L., and L. M. DiNicola. 2019. "The Brain's Default Network: Updated Anatomy, Physiology and Evolving Insights." *Nature Reviews Neuroscience* 20: 593–608. <https://doi.org/10.1038/s41583-019-0212-7>.

Byrd, R. H., P. Lu, J. Nocedal, and C. Zhu. 1995. "A Limited Memory Algorithm for Bound Constrained Optimization." *SIAM Journal on Scientific Computing* 16: 1190–1208.

Canales-Rodríguez, E. J., S. Alonso-Lana, N. Verdolini, et al. 2021. "Age- and Gender-Related Differences in Brain Tissue Microstructure Revealed by Multi-Component T2 Relaxometry." *Neurobiology of Aging* 106: 68–79.

Chamberlin, N., and C. Saper. 1994. "Topographic Organization of Respiratory Responses to Glutamate Microstimulation of the Parabrachial Nucleus in the Rat." *Journal of Neuroscience* 14: 6500–6510.

Chen, Y., T. Chen, and R. Hou. 2022. "Locus Coeruleus in the Pathogenesis of Alzheimer's Disease: A Systematic Review." *Alzheimer's & Dementia: Translational Research & Clinical Interventions* 8: e12257.

Cole, M. W., D. S. Bassett, J. D. Power, T. S. Braver, and S. E. Petersen. 2014. "Intrinsic and Task-Evoked Network Architectures of the Human Brain." *Neuron* 83: 238–251.

Dawe, R. J., D. A. Bennett, J. A. Schneider, S. K. Vasireddi, and K. Arfanakis. 2009. "Postmortem MRI of Human Brain Hemispheres: T2 Relaxation Times During Formaldehyde Fixation." *Magnetic Resonance in Medicine* 61: 810–818.

De Marco, M., and A. Venneri. 2018. "Volume and Connectivity of the Ventral Tegmental Area Are Linked to Neurocognitive Signatures of Alzheimer's Disease in Humans." *Journal of Alzheimer's Disease* 63: 167–180.

DeLong, E. R., D. M. DeLong, and D. L. Clarke-Pearson. 1988. "Comparing the Areas Under Two or More Correlated Receiver

- Operating Characteristic Curves: A Nonparametric Approach." *Biometrics* 44: 837. <https://doi.org/10.2307/2531595>.
- Demertzi, A., E. Tagliazucchi, S. Dehaene, et al. 2019. "Human Consciousness Is Supported by Dynamic Complex Patterns of Brain Signal Coordination." *Science Advances* 5: eaat7603.
- Dempster, A. P., N. M. Laird, and D. B. Rubin. 1977. "Maximum Likelihood From Incomplete Data via the EM Algorithm." *Journal of the Royal Statistical Society. Series B, Statistical Methodology* 39: 1–22.
- Donatelli, G., A. Emmi, M. Costagli, et al. 2023. "Brainstem Anatomy With 7-T MRI: In Vivo Assessment and Ex Vivo Comparison." *European Radiology Experimental* 7: 71.
- Edlow, B. L., C. Chatelle, C. A. Spencer, et al. 2017. "Early Detection of Consciousness in Patients With Acute Severe Traumatic Brain Injury." *Brain* 140: 2399–2414.
- Edlow, B. L., J. Claassen, N. D. Schiff, and D. M. Greer. 2021. "Recovery From Disorders of Consciousness: Mechanisms, Prognosis and Emerging Therapies." *Nature Reviews. Neurology* 17: 135–156.
- Edlow, B. L., R. L. Haynes, E. Takahashi, et al. 2013. "Disconnection of the Ascending Arousal System in Traumatic Coma." *Journal of Neuropathology & Experimental Neurology* 72: 505–523.
- Edlow, B. L., A. Mareyam, A. Horn, et al. 2019. "7 Tesla MRI of the Ex Vivo Human Brain at 100 Micron Resolution." *Scientific Data* 6: 244.
- Edlow, B. L., J. A. McNab, T. Witzel, and H. C. Kinney. 2016. "The Structural Connectome of the Human Central Homeostatic Network." *Brain Connectivity* 6: 187–200.
- Edlow, B. L., M. Olchanyi, H. J. Freeman, et al. 2024. "Multimodal MRI Reveals Brainstem Connections That Sustain Wakefulness in Human Consciousness." *Science Translational Medicine* 16: eadj4303. <https://doi.org/10.1126/scitranslmed.adj4303>.
- Edlow, B. L., E. Takahashi, O. Wu, et al. 2012. "Neuroanatomic Connectivity of the Human Ascending Arousal System Critical to Consciousness and Its Disorders." *Journal of Neuropathology and Experimental Neurology* 71: 531–546.
- Fischer, D. B., A. D. Boes, A. Demertzi, et al. 2016. "A Human Brain Network Derived From Coma-Causing Brainstem Lesions." *Neurology* 87: 2427–2434.
- Fischl, B. 2012. "FreeSurfer." *NeuroImage* 62: 774–781.
- Fischl, B., D. H. Salat, E. Busa, et al. 2002. "Whole Brain Segmentation." *Neuron* 33: 341–355. [https://doi.org/10.1016/s0896-6273\(02\)00569-x](https://doi.org/10.1016/s0896-6273(02)00569-x).
- Fischl, B., D. H. Salat, A. J. W. van der Kouwe, et al. 2004. "Sequence-Independent Segmentation of Magnetic Resonance Images." *NeuroImage* 23: S69–S84.
- Fox, M. D., A. Z. Snyder, J. L. Vincent, M. Corbetta, D. C. Van Essen, and M. E. Raichle. 2005. "The Human Brain Is Intrinsically Organized Into Dynamic, Anticorrelated Functional Networks." *Proceedings of the National Academy of Sciences of the United States of America* 102: 9673–9678.
- Galgani, A., F. Lombardo, N. Martini, et al. 2023. "Magnetic Resonance Imaging Locus Coeruleus Abnormality in Amnesic Mild Cognitive Impairment Is Associated With Future Progression to Dementia." *European Journal of Neurology* 30: 32–46.
- Giacino, J. T., K. Kalmar, and J. Whyte. 2004. "The JFK Coma Recovery Scale-Revised: Measurement Characteristics and Diagnostic Utility. No Commercial Party Having a Direct Financial Interest in the Results of the Research Supporting This Article Has or Will Confer a Benefit Upon the Authors or Upon Any Organization With Which the Authors Are Associated." *Archives of Physical Medicine and Rehabilitation* 85: 2020–2029.
- Gibb, W. R., C. Q. Mountjoy, D. M. Mann, and A. J. Lees. 1989. "The Substantia Nigra and Ventral Tegmental Area in Alzheimer's Disease and Down's Syndrome." *Journal of Neurology, Neurosurgery, and Psychiatry* 52: 193–200.
- Glasser, M. F., T. S. Coalson, E. C. Robinson, et al. 2016. "A Multi-Modal Parcellation of Human Cerebral Cortex." *Nature* 536: 171–178.
- Hansen, J. Y., S. Cauzzo, K. Singh, et al. 2024. "Integrating Brainstem and Cortical Functional Architectures." *Nature Neuroscience* 27: 2500–2511.
- Heckemann, R. A., J. V. Hajnal, P. Aljabar, D. Rueckert, and A. Hammers. 2006. "Automatic Anatomical Brain MRI Segmentation Combining Label Propagation and Decision Fusion." *NeuroImage* 33: 115–126. <https://doi.org/10.1016/j.neuroimage.2006.05.061>.
- Horn, A., D. Ostwald, M. Reisert, and F. Blankenburg. 2014. "The Structural-Functional Connectome and the Default Mode Network of the Human Brain." *NeuroImage* 102: 142–151. <https://doi.org/10.1016/j.neuroimage.2013.09.069>.
- Huang, C., L. Huang, Y. Wang, et al. 2021. "6-Month Consequences of COVID-19 in Patients Discharged From Hospital: A Cohort Study." *Lancet* 397: 220–232.
- Iglesias, J. E., J. C. Augustinack, K. Nguyen, et al. 2015. "A Computational Atlas of the Hippocampal Formation Using Ex Vivo, Ultra-High Resolution MRI: Application to Adaptive Segmentation of In Vivo MRI." *NeuroImage* 115: 117–137.
- Iglesias, J. E., R. Insausti, G. Lerma-Usabiaga, et al. 2018. "A Probabilistic Atlas of the Human Thalamic Nuclei Combining Ex Vivo MRI and Histology." *NeuroImage* 183: 314–326.
- Iglesias, J. E., K. Van Leemput, P. Bhatt, et al. 2015. "Bayesian Segmentation of Brainstem Structures in MRI." *NeuroImage* 113: 184–195.
- Izzy, S., N. L. Mazwi, S. Martinez, et al. 2017. "Revisiting Grade 3 Diffuse Axonal Injury: Not All Brainstem Microbleeds Are Prognostically Equal." *Neurocritical Care* 27: 199–207.
- Jang, S. H., S. H. Kim, and M. K. Cho. 2023. "Relationship Between the Consciousness State and the Default Mode Network in Traumatic Brain Injury." *Journal of Integrative Neuroscience* 22: 37.
- Jang, S. H., and Y. H. Kwon. 2020. "The Relationship Between Consciousness and the Ascending Reticular Activating System in Patients With Traumatic Brain Injury." *BMC Neurology* 20: 375.
- Jang, S. H., S. S. Yeo, M. J. Cho, and W. K. Chung. 2024. "Correlation Between Thalamocortical Tract and Default Mode Network With Consciousness Levels in Hypoxic-Ischemic Brain Injury Patients: A Comparative Study Using the Coma Recovery Scale-Revised." *Medical Science Monitor* 30: e943802.
- Ji, X., H. Wang, M. Zhu, et al. 2020. "Brainstem Atrophy in the Early Stage of Alzheimer's Disease: A Voxel-Based Morphometry Study." *Brain Imaging and Behavior* 15: 49–59. <https://doi.org/10.1007/s11682-019-00231-3>.
- Kinney, H. C., and R. L. Haynes. 2019. "The Serotonin Brainstem Hypothesis for the Sudden Infant Death Syndrome." *Journal of Neuropathology & Experimental Neurology* 78: 765–779. <https://pubmed.ncbi.nlm.nih.gov/31397480>.
- Kotrotsou, A., D. A. Bennett, J. A. Schneider, et al. 2014. "Ex Vivo MR Volumetry of Human Brain Hemispheres." *Magnetic Resonance in Medicine* 71: 364–374.
- Lambert, C., A. Lutti, G. Helms, R. Frackowiak, and J. Ashburner. 2013. "Multiparametric Brainstem Segmentation Using a Modified Multivariate Mixture of Gaussians." *NeuroImage: Clinical* 2: 684–694.
- Lechanoine, F., T. Jacquesson, J. Beaujoin, et al. 2021. "WIKIBrainStem: An Online Atlas to Manually Segment the Human Brainstem at the Mesoscopic Scale From Ultrahigh Field MRI." *NeuroImage* 236: 118080. <https://doi.org/10.1016/j.neuroimage.2021.118080>.

- Lee, J., Y. Tseng, L. Liu, et al. 2007. "A 2-D Automatic Segmentation Scheme for Brainstem and Cerebellum Regions in Brain MR Imaging." In *Fourth International Conference on Fuzzy Systems and Knowledge Discovery (FSKD 2007)*, 270–274. IEEE.
- Lee, J. H., J. Ryan, C. Andreescu, H. Aizenstein, and H. K. Lim. 2015. "Brainstem Morphological Changes in Alzheimer's Disease." *Neuroreport* 26: 411–415.
- Lee, J.-D., N.-W. Wang, C.-H. Huang, L.-C. Liu, and C.-S. Lu. 2005. "A Segmentation Scheme of Brainstem and Cerebellum Using Scale-Based Fuzzy Connectedness and Deformable Contour Model." In *2005 IEEE Engineering in Medicine and Biology 27th Annual Conference*, 459–462. IEEE.
- Li, J., W. H. Curley, B. Guerin, et al. 2021. "Mapping the Subcortical Connectivity of the Human Default Mode Network." *NeuroImage* 245: 118758.
- Luft, A. R. 1999. "Patterns of Age-Related Shrinkage in Cerebellum and Brainstem Observed In Vivo Using Three-Dimensional MRI Volumetry." *Cerebral Cortex* 9: 712–721.
- Mayer, D. J., T. L. Wolfle, H. Akil, B. Carder, and J. C. Liebeskind. 1971. "Analgesia From Electrical Stimulation in the Brainstem of the Rat." *Science* 174: 1351–1354.
- McNab, J. A., S. Jbabdi, S. C. L. Deoni, G. Douaud, T. E. J. Behrens, and K. L. Miller. 2009. "High Resolution Diffusion-Weighted Imaging in Fixed Human Brain Using Diffusion-Weighted Steady State Free Precession." *NeuroImage* 46: 775–785. <https://doi.org/10.1016/j.neuroimage.2009.01.008>.
- Medaglia, J. D., M.-E. Lynall, and D. S. Bassett. 2015. "Cognitive Network Neuroscience." *Journal of Cognitive Neuroscience* 27: 1471–1491.
- Miyoshi, F., T. Ogawa, S.-i. Kitao, et al. 2013. "Evaluation of Parkinson Disease and Alzheimer Disease With the Use of Neuromelanin MR Imaging and ¹²³I-Metaiodobenzylguanidine Scintigraphy." *American Journal of Neuroradiology* 34: 2113–2118.
- Morales, M., and E. B. Margolis. 2017. "Ventral Tegmental Area: Cellular Heterogeneity, Connectivity and Behaviour." *Nature Reviews. Neuroscience* 18: 73–85.
- Mufson, E. J., D. C. Mash, and L. B. Hersh. 1988. "Neurofibrillary Tangles in Cholinergic Pedunculopontine Neurons in Alzheimer's Disease." *Annals of Neurology* 24: 623–629.
- Ng, A., and M. Jordan. 2001. "On Discriminative vs. Generative Classifiers: A Comparison of Logistic Regression and Naive Bayes." In *Advances in Neural Information Processing Systems*, edited by T. Dietterich, S. Becker, and Z. Ghahramani, 14. MIT Press.
- Nigro, S., A. Cerasa, G. Zito, et al. 2014. "Fully Automated Segmentation of the Pons and Midbrain Using Human T1 MR Brain Images." *PLoS One* 9: e85618.
- Olszewski, J., and D. Baxter. 1954. "Cytoarchitecture of the Human Brainstem." *Journal of Comparative Neurology* 101: 825.
- Parvizi, J. 2001. "Consciousness and the Brainstem." *Cognition* 79: 135–160. [https://doi.org/10.1016/s0010-0277\(00\)00127-x](https://doi.org/10.1016/s0010-0277(00)00127-x).
- Parvizi, J., and A. R. Damasio. 2003. "Neuroanatomical Correlates of Brainstem Coma." *Brain* 126: 1524–1536.
- Parvizi, J., G. W. Van Hoesen, and A. Damasio. 1998. "Severe Pathological Changes of Parabrachial Nucleus in Alzheimer's Disease." *Neuroreport* 9: 4151–4154.
- Parvizi, J., G. W. Van Hoesen, and A. Damasio. 2000. "Selective Pathological Changes of the Periaqueductal Gray Matter in Alzheimer's Disease." *Annals of Neurology* 48: 344–353.
- Parvizi, J., G. W. Van Hoesen, and A. Damasio. 2001. "The Selective Vulnerability of Brainstem Nuclei to Alzheimer's Disease." *Annals of Neurology* 49: 53–66.
- Patenaude, B., S. M. Smith, D. N. Kennedy, and M. Jenkinson. 2011. "A Bayesian Model of Shape and Appearance for Subcortical Brain Segmentation." *NeuroImage* 56: 907–922.
- Paxinos, G., H. Xu-Feng, G. Sengul, and C. Watson. 2012. "Organization of Brainstem Nuclei." In *The Human Nervous System*, 260–327. Elsevier.
- Petersen, R. C., P. S. Aisen, L. A. Beckett, et al. 2010. "Alzheimer's Disease Neuroimaging Initiative (ADNI)." *Neurology* 74: 201–209.
- Pohl, K. M., J. Fisher, W. E. L. Grimson, R. Kikinis, and W. M. Wells. 2006. "A Bayesian Model for Joint Segmentation and Registration." *NeuroImage* 31: 228–239.
- Puonti, O., J. E. Iglesias, and K. Van Leemput. 2016. "Fast and Sequence-Adaptive Whole-Brain Segmentation Using Parametric Bayesian Modeling." *NeuroImage* 143: 235–249.
- Quester, R., and R. Schröder. 1997. "The Shrinkage of the Human Brain Stem During Formalin Fixation and Embedding in Paraffin." *Journal of Neuroscience Methods* 75: 81–89.
- Reynolds, D. V. 1969. "Surgery in the Rat During Electrical Analgesia Induced by Focal Brain Stimulation." *Science* 164: 444–445.
- Robson, M. D., J. C. Gore, and R. T. Constable. 1997. "Measurement of the Point Spread Function in MRI Using Constant Time Imaging." *Magnetic Resonance in Medicine* 38: 733–740.
- Rüb, U., K. Stratmann, H. Heinsen, et al. 2016. "The Brainstem Tau Cytoskeletal Pathology of Alzheimer's Disease: A Brief Historical Overview and Description of Its Anatomical Distribution Pattern, Evolutional Features, Pathogenetic and Clinical Relevance." *Current Alzheimer Research* 13: 1178–1197.
- Saper, C. B., T. E. Scammell, and J. Lu. 2005. "Hypothalamic Regulation of Sleep and Circadian Rhythms." *Nature* 437: 1257–1263.
- Saygin, Z. M., D. Kliemann, J. E. Iglesias, et al. 2017. "High-Resolution Magnetic Resonance Imaging Reveals Nuclei of the Human Amygdala: Manual Segmentation to Automatic Atlas." *NeuroImage* 155: 370–382.
- Schiff, N. D., and F. Plum. 2000. "The Role of Arousal and "Gating" Systems in the Neurology of Impaired Consciousness." *Journal of Clinical Neurophysiology* 17: 438–452. <https://doi.org/10.1097/00004691-200009000-00002>.
- Sclocco, R., F. Beissner, M. Bianciardi, J. R. Polimeni, and V. Napadow. 2018. "Challenges and Opportunities for Brainstem Neuroimaging With Ultrahigh Field MRI." *NeuroImage* 168: 412–426.
- Shepherd, T. M., J. J. Flint, P. E. Thelwall, et al. 2009. "Postmortem Interval Alters the Water Relaxation and Diffusion Properties of Rat Nervous Tissue—Implications for MRI Studies of Human Autopsy Samples." *NeuroImage* 44: 820–826.
- Sheth, K. N., M. H. Mazurek, M. M. Yuen, et al. 2021. "Assessment of Brain Injury Using Portable, Low-Field Magnetic Resonance Imaging at the Bedside of Critically Ill Patients." *JAMA Neurology* 78: 41–47.
- Simic, G., G. Stanic, M. Mladinov, N. Jovanov-Milosevic, I. Kostovic, and P. R. Hof. 2009. "Does Alzheimer's Disease Begin in the Brainstem?" *Neuropathology and Applied Neurobiology* 35: 532–554.
- Smith, S. M., M. Jenkinson, M. W. Woolrich, et al. 2004. "Advances in Functional and Structural MR Image Analysis and Implementation as FSL." *NeuroImage* 23: S208–S219. <https://doi.org/10.1016/j.neuroimage.2004.07.051>.
- Snider, S. B., Y. G. Bodien, M. Bianciardi, E. N. Brown, O. Wu, and B. L. Edlow. 2019. "Disruption of the Ascending Arousal Network in Acute Traumatic Disorders of Consciousness." *Neurology* 93: e1281–e1287.
- Snider, S. B., Y. G. Bodien, A. Frau-Pascual, M. Bianciardi, A. S. Foulkes, and B. L. Edlow. 2020. "Ascending Arousal Network Connectivity During Recovery From Traumatic Coma." *NeuroImage: Clinical* 28: 102503.

- Snider, S. B., J. Hsu, R. R. Darby, et al. 2020. "Cortical Lesions Causing Loss of Consciousness Are Anticorrelated With the Dorsal Brainstem." *Human Brain Mapping* 41: 1520–1531.
- Song, Y. J. C., M. S. Korgaonkar, L. V. Armstrong, S. Eagles, L. M. Williams, and S. M. Grieve. 2014. "Tractography of the Brainstem in Major Depressive Disorder Using Diffusion Tensor Imaging." *PLoS One* 9: e84825.
- Sporns, O., G. Tononi, and R. Kötter. 2005. "The Human Connectome: A Structural Description of the Human Brain." *PLoS Computational Biology* 1: e42.
- Takahashi, J., T. Shibata, M. Sasaki, et al. 2015. "Detection of Changes in the Locus Coeruleus in Patients With Mild Cognitive Impairment and Alzheimer's Disease: High-Resolution Fast Spin-Echo T1-Weighted Imaging." *Geriatrics & Gerontology International* 15: 334–340.
- Tao, J., W. Zhang, D. Wang, et al. 2015. "Susceptibility Weighted Imaging in the Evaluation of Hemorrhagic Diffuse Axonal Injury." *Neural Regeneration Research* 10: 1879.
- Teasdale, G., and B. Jennett. 1974. "Assessment of Coma and Impaired Consciousness." *Lancet* 304: 81–84.
- Tregidgo, H. F. J., S. Soskic, J. Althonayan, et al. 2023. "Accurate Bayesian Segmentation of Thalamic Nuclei Using Diffusion MRI and an Improved Histological Atlas." *NeuroImage* 274: 120129.
- Uematsu, M., A. Nakamura, M. Ebashi, K. Hirokawa, R. Takahashi, and T. Uchihara. 2018. "Brainstem Tau Pathology in Alzheimer's Disease Is Characterized by Increase of Three Repeat Tau and Independent of Amyloid β ." *Acta Neuropathologica Communications* 6, no. 1: 1.
- Valenza, G., R. Sclocco, A. Duggento, et al. 2019. "The Central Autonomic Network at Rest: Uncovering Functional MRI Correlates of Time-Varying Autonomic Outflow." *NeuroImage* 197: 383–390. <https://doi.org/10.1016/j.neuroimage.2019.04.075>.
- Van Essen, D. C., S. M. Smith, D. M. Barch, T. E. J. Behrens, E. Yacoub, and K. Ugurbil. 2013. "The WU-Minn Human Connectome Project: An Overview." *NeuroImage* 80: 62–79.
- Van Leemput, K. 2009. "Encoding Probabilistic Brain Atlases Using Bayesian Inference." *IEEE Transactions on Medical Imaging* 28: 822–837.
- Van Leemput, K., F. Maes, D. Vandermeulen, and P. Suetens. 1999. "Automated Model-Based Tissue Classification of MR Images of the Brain." *IEEE Transactions on Medical Imaging* 18: 897–908.
- Wasserthal, J., P. Neher, and K. H. Maier-Hein. 2018. "TractSeg—Fast and Accurate White Matter Tract Segmentation." *NeuroImage* 183: 239–253.
- Wells, W. M., W. E. L. Grimson, R. Kikinis, and F. A. Jolesz. 1996. "Adaptive Segmentation of MRI Data." *IEEE Transactions on Medical Imaging* 15: 429–442.
- Wong, M.-L., M. A. Kling, P. J. Munson, et al. 2000. "Pronounced and Sustained Central Hypertrophic Function in Major Depression With Melancholic Features: Relation to Hypercortisolism and Corticotropin-Releasing Hormone." *Proceedings of the National Academy of Sciences of the United States of America* 97: 325–330.
- Xiong, Q., Y. Wang, Z. Wang, et al. 2022. "Relationship Between Consciousness Level and Perfusion Computed Tomography in Patients With Prolonged Disorders of Consciousness." *Aging* 14: 9668–9678.
- Yendiki, A., M. Aggarwal, M. Axer, A. F. D. Howard, A.-M. v. C. van Walsum, and S. N. Haber. 2022. "Post Mortem Mapping of Connectional Anatomy for the Validation of Diffusion MRI." *NeuroImage* 256: 119146.
- Yeo, B. T. T., F. M. Krienen, J. Sepulcre, et al. 2011. "The Organization of the Human Cerebral Cortex Estimated by Intrinsic Functional Connectivity." *Journal of Neurophysiology* 106: 1125–1165. <https://pubmed.ncbi.nlm.nih.gov/21653723>.

Zhang, J., R.-L. Wei, G.-P. Peng, et al. 2017. "Correlations Between Diffusion Tensor Imaging and Levels of Consciousness in Patients With Traumatic Brain Injury: A Systematic Review and Meta-Analysis." *Scientific Reports* 7: 2793.

Supporting Information

Additional supporting information can be found online in the Supporting Information section. **Video S1:** Fly-through visualization of the adaptive probabilistic atlas mesh that encodes locations and intensity distributions of ascending arousal network nuclei in the brainstem. The mesh axis is displayed in the coronal plane. DR, dorsal raphe; LC, locus coeruleus; LDTg, laterodorsal tegmental nucleus; MnR, median raphe; mRt, midbrain reticular formation; PAG, periaqueductal gray; PBC, parabrachial complex; PnO, pontis oralis; PTg, pedunculotegmental nucleus; VTA, ventral tegmental area. The full video can also be accessed through [Zenodo](#). **Figure S1:** Axial tyrosine hydroxylase section in the midbrain (top left) and tryptophan hydroxylase section in the pons (bottom left) with delineated boundaries of AAN nuclei, as compared to corresponding contrast boundaries in 200 μ m FLASH images. **Figure S2:** Axial cross-section of representative subject from the TBI dataset with hemorrhagic lesions in the basis pontis (red arrows). SWI (right) provides greater sensitivity to such regions of hemorrhagic products from diffuse axonal injury than do standard structural sequences such as T1 (left) (Tao et al. 2015). **Figure S3:** Axial cross-sections of the midbrain (left) and pons (right) of a representative T1 MRI scan from the dataset used for accuracy analysis. We observed that a subset of AAN nuclei, such as the PAG, mRt, VTA, MnR and DR, possess enough T1 contrast at their neuroanatomic boundaries for reliable manual annotation (solid white line). The rest of the AAN nuclei were manually annotated with respect to the location of the aforementioned AAN nuclei, and with guidance from brainstem atlases. **Figure S4:** Representative T1 axial sections of all manual annotations for the 10 control subjects and 10 TBI patients used for assessment of segmentation (outlined) accuracy overlaid with corresponding Bayesian segmentations (semi-transparent). **Figure S5:** Representative SWI sagittal (top) and axial (bottom) sections of all patients from the TBI dataset. Outlined in red are the SWI scans excluded from correlation analysis due to the presence of significant SWI motion artifacts. **Figure S6:** Axial sections at the level of the rostral midbrain (left), caudal midbrain (middle), and mid-pons (right) for a probabilistic atlas mesh trained on three ex vivo brain specimens (top row), and the "complete" atlas mesh with five ex vivo brain specimens (bottom row). Both atlases show minimal change in mesh configuration and posterior label morphology for each AAN nucleus, indicating convergence of the atlas with five ex vivo specimens. **Figure S7:** Relationship between the spatial volume of each individual AAN nucleus with respect to the fixation-to-imaging duration of each ex vivo brain specimen. **Table S1:** Information of demographics control subjects used for accuracy analysis. **Table S2:** Information of demographics and clinical examination findings for all TBI patients. CRSR-T, total coma recovery scale-revised; GCS-T, total Glasgow Coma Scale score; MCS–, minimally conscious state without evidence of language function; MCS+, minimally conscious state with evidence of language function; MVA, motor vehicle accident; Ped vs. car, pedestrian versus car; PTCS, post-traumatic confusional state; VS, vegetative state. Further study and subject information can be found in (Edlow et al. 2017). **Table S3:** Demographic information for all HCP subjects used for test–retest analysis. Exact ages for subjects are not included due to HCP de-identification policies. The provided inter-scan duration (in months) is provided by HCP according to the following rules. 2: 1–2 month duration, 3: 3-month duration, 4: 4-month duration, 5: 5-month duration, 6: 6-month duration, 7: 7-month duration, 8: 8–10 month duration, 11: 11-month duration. Subject 179548 was excluded from analysis due to missing retest structural scans.